

Cyanate Formation via Photolytic Splitting of Dinitrogen

Bastian Schluschaß, Jan-Hendrik Borter,[#] Severine Rupp,[#] Serhiy Demeshko, Christian Herwig, Christian Limberg, Nicholas A. Maciulis, Jessica Schneider, Christian Würtele, Vera Krewald,^{*} Dirk Schwarzer,^{*} and Sven Schneider^{*}

Cite This: JACS Au 2021, 1, 879–894



Read Online

ACCESS |



Metrics & More



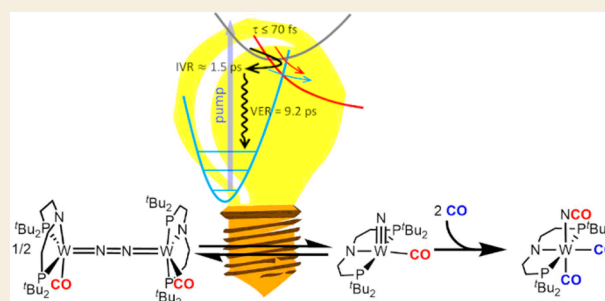
Article Recommendations



Supporting Information

ABSTRACT: Light-driven N₂ cleavage into molecular nitrides is an attractive strategy for synthetic nitrogen fixation. However, suitable platforms are rare. Furthermore, the development of catalytic protocols via this elementary step suffers from poor understanding of N–N photosplitting within dinitrogen complexes, as well as of the thermochemical and kinetic framework for coupled follow-up chemistry. We here present a tungsten pincer platform, which undergoes fully reversible, thermal N₂ splitting and reverse nitride coupling, allowing for experimental derivation of thermodynamic and kinetic parameters of the N–N cleavage step. Selective N–N splitting was also obtained photolytically. DFT computations allocate the productive excitations within the {WNNW} core. Transient absorption spectroscopy shows ultrafast repopulation of the electronic ground state. Comparison with ground-state kinetics and resonance Raman data support a pathway for N–N photosplitting via a nonstatistically vibrationally excited ground state that benefits from vibronically coupled structural distortion of the core. Nitride carbonylation and release are demonstrated within a full synthetic cycle for trimethylsilylcyanate formation directly from N₂ and CO.

KEYWORDS: Nitrogen Fixation, Nitride, N₂ Splitting, Photochemistry, Carbonylation



INTRODUCTION

After the seminal report of Laplaza and Cummins in 1995, the splitting of dinitrogen into molecular nitrido complexes has evolved as a synthetic strategy to nitrogen fixation at ambient conditions.^{1–4} Catalytic ammonia formation that commences with full N–N bond rupture, followed by proton-coupled electron transfer (PCET) steps, resembles the mechanism of the heterogeneously catalyzed *Haber–Bosch* process.^{5,6} Such a dissociative mechanism was recently proposed by Nishibayashi and co-workers for the currently most active class of homogeneous catalysts, which are Mo pincer complexes that mediate N₂ fixation with activities up to TON_{max} = 4350 and TOF_{max} = 117 min^{–1} using SmI₂/H₂O as a PCET reductant.^{7,8} Alternatively, nitride formation potentially offers an entry to subsequent C–N bond formation.^{3,4,9} Several groups demonstrated the suitability of dissociative mechanistic scenarios, e.g., to synthesize organic nitriles from N₂, within stepwise, cyclic reaction schemes (“synthetic cycles”).^{10–13} However, truly catalytic protocols that allow for the direct transformation of N₂ to organic products remain unknown to date.

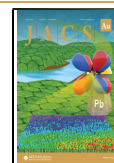
The thermochemical challenge of the dissociative approach to N₂ fixation arises from the extraordinarily strong N–N triple bond (BDE = 941 kJ·mol^{–1}),^{3,4} which needs to be counterbalanced by the formed M–N bonds. In consequence, C–N bond formation and N-transfer requires quite reactive reagents, such as strong electrophiles that are often incompatible with

the reductive conditions of N₂ activation. Photolytic N₂ splitting could be an attractive alternative to circumvent the thermochemical constraints and drive endothermic N₂ cleavage toward more reactive nitrides.¹⁴ However, platforms that were demonstrated to undergo photodriven N₂ splitting into molecular nitrides are rare (Figure 1).^{15–21} For almost all of them, the underlying photophysics that enable light-driven N–N cleavage are yet to be systematically examined.^{22–27} Advances for both thermally and light driven N₂ cleavage still suffer from a relatively poor understanding of structure–reactivity relationships.

In the past years, we examined thermally, electrochemically, and photochemically driven splitting of dinitrogen into molecular nitrides with group 6 and 7 pincer complexes.^{20,28–32} Like other systems that give terminal nitrides as N₂ cleavage products,^{2,7,33–36} dinuclear, $\mu^2\text{:}\eta^1\text{:}\eta^1\text{-N}_2$ bridged complexes were identified as key intermediates.^{20,29–31} Based on a covalent bonding model for the {MNNM} core,^{37,38} Cummins and co-workers qualitatively rationalized the N₂

Received: March 13, 2021

Published: May 20, 2021



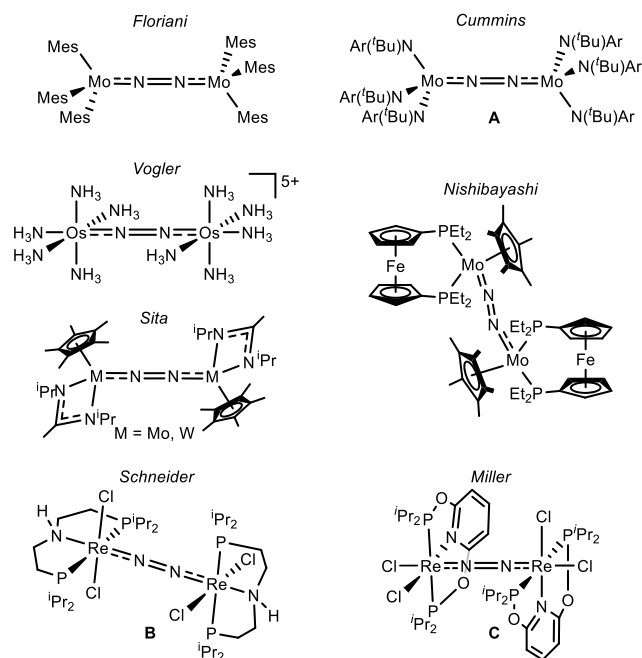


Figure 1. N_2 -bridged complexes that undergo photolytic cleavage into nitrides (Ar = $C_6H_3-3,5-Me_2$).^{15–21}

splitting reactivity of his *pseudo*-tetrahedral platform (Figure 1, A) by simple molecular orbital (MO) considerations.² Transfer to idealized D_{4h} symmetry expands this picture to the emerging class of metal-pincer complexes that mediate N_2 splitting (Figure 2).^{3,4} As a general feature, the precursors to N_2

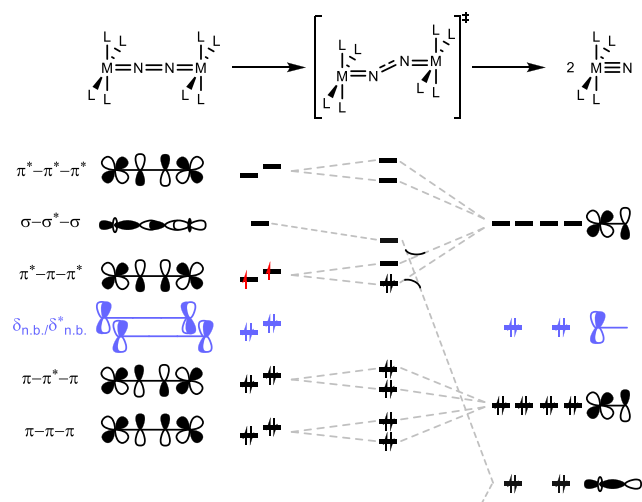


Figure 2. Qualitative molecular orbital correlation diagram for the splitting of $\mu^2\text{-}\eta^1\text{:}\eta^1\text{-}N_2$ bridged complexes with D_{4h} symmetry into terminal nitrides.

splitting exhibit electronic ground state configurations with 10 electrons in the {MNNM} π -MO manifold, such as $[(N_2)\{ReCl(PNP)\}_2]$ (D, $\pi_1^4\pi_2^4\delta_1^2\delta_2^2\pi_3^2$) or $[(N_2)\{MCl(HPNP)\}_2]^{2+}$ ($\pi_1^4\pi_2^4\delta_1^1\delta_2^1\pi_3^2$), respectively (M = Mo, W; PNP = $N(CH_2CH_2P^tBu)_2$).^{28–31} Full N–N cleavage is associated with an electronic rearrangement from the $\pi^*-\pi-\pi^*$ to the N–N σ^* MO via a zigzag transition state of the {MNNM} core. So far, this simple picture has proven fully consistent with computational electronic structure

treatment of related systems.^{7,21,28–32,35,36} However, several aspects of thermally and photochemically driven N–N cleavage are yet to be addressed:

- Both strongly activated N_2 complexes and the terminal nitride products can exhibit high degrees of covalent M–N bonding.^{39,40} The actual extent of charge transfer that is associated with cleavage of the N–N bond is surprisingly ill-defined. N_2 splitting of complexes incorporating the common spectroscopic probe CO,⁴¹ which is sensitive to electronic changes at the metal center, has not been reported, to date.
- Platforms that undergo N–N splitting generally exhibit strongly σ - and/or π -donating ligands that mix with the frontier orbitals of the {MNNM} core.^{29,42} Auxiliary ligand effects, e.g. from π -acceptors, on the thermodynamics and kinetics of N_2 cleavage need to be systematically explored.
- Only one photoactive complex (Figure 1, A) has been previously examined by transient absorption spectroscopy.²² The authors attributed photodriven N–N cleavage to vibrationally hot ground state reactivity. The applicability of these findings to other systems remains unknown.

We here report the synthesis of the CO-ligated complex $[(N_2)\{W(CO)(PNP)\}_2]$, which is the first compound that undergoes fully reversible splitting into molecular nitride complexes. The endothermic reaction can alternatively be driven by photolysis in the visible range. The photochemistry was examined by transient spectroscopy and quantum chemical treatment, and the reactivity could be utilized to drive a full synthetic cycle for isocyanate formation from N_2 and CO.

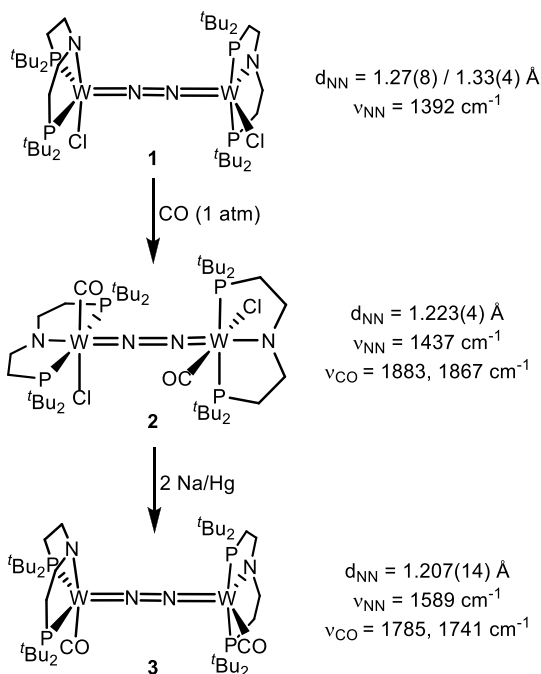
RESULTS

Syntheses and Electronic Structures of N_2 Bridged Complexes

The reaction of $[(N_2)\{WCl(PNP)\}_2]$ (1)³¹ with CO (1 atm) results in quantitative formation of $[(N_2)\{WCl(CO)(PNP)\}_2]$ (2) (Scheme 1) within 20 min. Longer reaction times lead to loss of N_2 and formation of $[WCl(CO)_2(PNP)]$ (*vide infra*). The 1H NMR spectrum of complex 2 features four signals for the tBu -groups as expected for a C_2 symmetric structure, like that of parent 1. Both sets of phosphorus atoms incidentally coincide as one $^{31}P\{^1H\}$ NMR resonance ($\delta_P = 65.9$ ppm), which was confirmed by ^{31}P HMBC spectroscopy. Conservation of the N_2 -bridge is evidenced by the $^{15}N\{^1H\}$ NMR spectrum of a $^{15}N_2$ labeled sample ($\delta_N = -0.69$ ppm; $^1J_{NW} = 70$ Hz). The idealized C_2 symmetric molecular structure was also found in the solid state (Figure 3). In comparison with 1, CO coordination results in slight contraction of the N–N bond ($\Delta d_{NN} = -0.08$ Å)⁴³ and a bathochromic shift of the N–N stretching frequency ($\Delta\nu = +45$ cm^{-1}), which is attributed to competing backbonding to the CO and N_2 ligands, respectively. All attempts to obtain analogous isonitride complexes resulted in W– N_2 dissociation.

Reduction of 2 with Na/Hg or $CoCp^*_2$ (2 equiv), respectively, gives deep red $[(N_2)\{W(CO)(PNP)\}_2]$ (3) in isolated yields up to 60% (Scheme 1). In the solid state, the structure of complex 3 resembles that of 1, where Cl is replaced by CO (Figure 3). The pyramidally coordinated tungsten ions ($\tau_5 = 0.23$)⁴⁴ are linearly bridged by the N_2 ligand in the apical sites. As was found for the chloro analogues

Scheme 1. Synthesis and Selected Spectroscopic and Structural Parameters of Complexes 2 and 3



$[(N_2)\{MCl(PNP)\}_2]$ (M = W (1), Mo, Re),^{29–31} the two $\{W(CO)(PNP)\}$ fragments are twisted with respect to each other by about 87° presumably due to the steric bulk of the $t\text{Bu}$ -substituents.

The approximate C_2 symmetry of 3 in the solid state is in line with the number of ^1H NMR resonances in solution. All signals are sharp, but paramagnetically shifted over a wide range ($\Delta\delta = 31$ ppm). The absence of a $^{31}\text{P}\{^1\text{H}\}$ NMR signal further indicates an open-shell ground state. This interpretation was confirmed by SQUID magnetometry. The magnetic moment at room temperature ($\mu_{\text{eff}} = 2.3 \pm 0.1 \mu_B$) supports two unpaired electrons with considerable orbital contributions. Below 150 K, the $\chi_M T$ vs T curve features temperature-independent susceptibility. The magnetic data could be fitted to a zero-field splitting (ZFS) spin-Hamiltonian ($S = 1$, $g_{\text{av}} = 1.74$) with large axial ZFS ($D = 407 \text{ cm}^{-1}$), which is in line with a triplet ground state that is energetically well separated due to large spin-orbit coupling (SOC).^{17,45–48} DFT computations with the PBE functional confirmed the triplet ground state of complex 3. However, the corresponding closed-shell solution was found only $1.1 \text{ kcal}\cdot\text{mol}^{-1}$ higher in energy suggesting multireference character of the ground-state wave function, which is supported by the magnetic properties yet not sufficiently expressed by DFT computations. Note that a similar spin state splitting was found with hybrid functionals, like PBE0 ($2.0 \text{ kcal}\cdot\text{mol}^{-1}$), suggesting that the spin state energetics are not very sensitive to the extent of exact exchange admixture, as was previously found by Harvey and Poli for tungsten complexes.^{49,50} For both spin states, additional conformers of the pincer ligand were found close in energy (see Scheme 2 and the SI), as an expression of the high flexibility of the saturated aliphatic backbone. The computed lowest conformer of 3 closely resembles the experimental structure in the crystal, while a different conformer (3') was

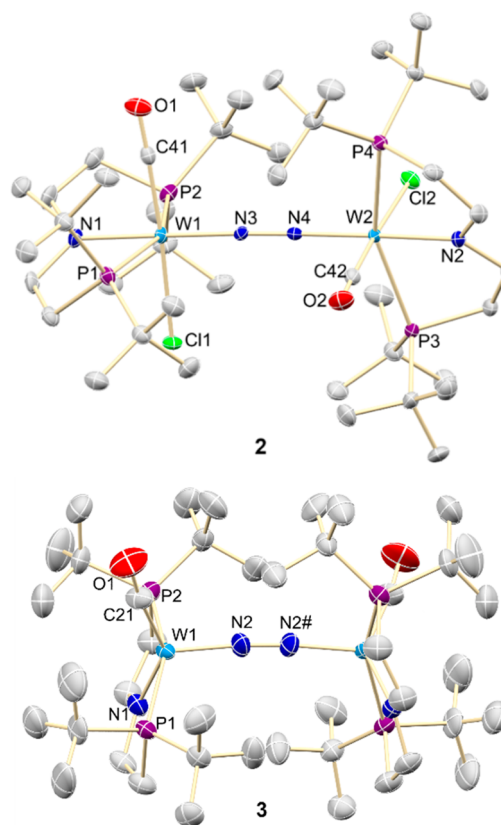
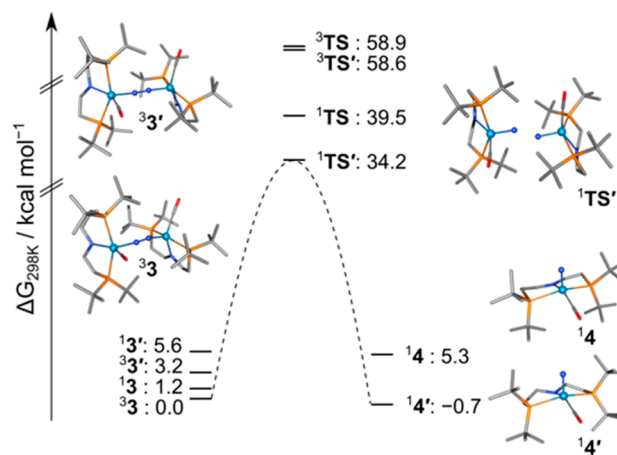


Figure 3. Molecular structures of 2 (top) and 3 (bottom) in the crystal from X-ray diffraction. Thermal ellipsoids are shown at 50% and 25% probability level, respectively. All hydrogen atoms were omitted for clarity. Selected bond lengths [Å] and angles [°] for 2 [N3–N4 1.223(4), W1–N1 2.032(3), W1–N3 1.870(3), W2–N2 2.023(3), W2–N4 1.872(3); W1–N3–N4 174.2(3), W2–N4–N3 174.2(3), N1–W1–N3 177.38(13), N2–W2–N4 174.40(13), P1–W1–P2 155.22(3), P3–W2–P4 157.19(3), C41–W1–Cl1 176.5(2), C42–W2–Cl2 176.09(15)] and 3 [N2–N2# 1.207(14), W1–C21 1.956(14)/1.97(2), W1–N1 2.043(10)/2.04(2), W1–N2 1.869(7), W1–P1 2.485(3)/2.398(14), W1–P2 2.435(4)/2.517(17); C21–W1–N1 140.9(9)/156(4), P1–W1–P2 154.79(13)/151.7(6), W1–N2–N2# 173.7(7)].

Scheme 2. Computed Energy Profile for the Thermal Splitting of 3 into 4 at Room Temperatures^a



^aAll values are given in $\text{kcal}\cdot\text{mol}^{-1}$ referenced to the triplet ground-state and are not drawn to scale.

found 1.1 and 5.3 kcal·mol^{−1} higher in free energy in the triplet and singlet states, respectively.

The reduced complex **3** exhibits a lower degree of N₂ activation than both parent complexes **1** and **2** (Scheme 1) as judged by the shorter N–N bond (3 $d_{\text{NN}} = 1.207(14)$ Å) and higher energy of the N–N stretching vibration (3 $\nu_{\text{NN}} = 1589$ cm^{−1}). On first sight, this might seem counterintuitive when comparing the bathochromically shifted CO stretching vibrations of **3** ($\nu_{\text{CO}} = 1785, 1741$ cm^{−1}) vs **2** ($\nu_{\text{CO}} = 1883, 1867$ cm^{−1}).⁵¹ However, according to the qualitative electronic structure considerations (Figure 2), complexes **1** and **2** both exhibit $\{\pi^8\delta^4\}$ closed-shell configurations of the $\{\text{WNNW}\}$ core.^{3,4} The $S = 1$ ground state of **3** is in line with the population of two orthogonal, nearly degenerate $\{\pi^*- \pi - \pi^*\}$ -MOs upon reduction. Their N–N bonding character reduces the degree of N₂ activation, which comes closer to, e.g., the $\{\pi^{10}\delta^4\}$ complex **D** ($d_{\text{NN}} = 1.202(10)$ Å) or complex **A** ($d_{\text{NN}} = 1.212(2)/1.217(2)$ Å, $\nu_{\text{NN}} = 1630$ cm^{−1}).^{2,16,30} Note that the different symmetry of **A** (S_6) leads to a $\{\pi^{10}\}$ configuration with closely related N₂ bonding that results from overall 10 electrons in the π -MO manifold and high-lying, vacant d-orbitals of δ symmetry.⁴ These qualitative electronic structure considerations are fully corroborated for **3** by the DFT computations. Importantly, the DFT results show significant backdonation from the δ orbitals to CO and, in addition, admixture of CO character in the π -manifold of the $\{\text{WNNW}\}$ unit (see the SI). Based on this picture, the significant reduction of the degree of N₂ activation is rationalized as an expression of a high degree of covalency in W–N bonding.

Thermally Driven Splitting of N₂

While **3** is stable at room temperature in solution for several days, heating ($T = 80$ °C) over several hours affords the pale blue nitrido complex $[\text{W}(\text{N})(\text{CO})(\text{PNP})]$ (**4**, Figure 4). NMR spectra of the diamagnetic N₂ cleavage product **4** are in

agreement with a square-pyramidal, C_s symmetric structure in solution. N₂ splitting was confirmed by thermolysis of a ¹⁵N₂ labeled sample ($\delta_{\text{N}} = 447$ ppm). The W≡N stretching vibration (ν_{WN}) was found at 998 cm^{−1} ($\nu_{\text{WN}}(^{15}\text{N-4}) = 973$ cm^{−1}), which is close to values found for related tungsten nitrido complexes.^{31,52}

N₂ splitting is associated with a distinct hypsochromic shift of the CO stretching frequency ($\nu_{\text{CO}} = 1883$ cm^{−1}) with respect to parent **3** ($\nu_{\text{CO}} = 1785, 1741$ cm^{−1}). The spectroscopic probe therefore supports a significant degree of metal to nitrogen charge transfer reflecting a reductive nature of N–N bond cleavage that leads from the N₂ bridged $\{\pi^{10}\delta^4\}$ triplet species to the closed-shell terminal nitrides.

The N₂ splitting reaction was monitored by ¹H NMR spectroscopy at four different temperatures between 75 and 105 °C (Figure 4). Interestingly, reaction progress terminates prior to full conversion, suggesting slow equilibration of forward N₂ splitting and reverse nitride coupling.^{53–60} This interpretation is supported by a control experiment which proved the formation of N₂ bridged complex **3** by ¹H NMR spectroscopy upon prolonged heating of independently prepared **4** under the exclusion of light. The kinetic data for the splitting of **3** could be fitted to an equilibrium model affording both thermodynamic and kinetic parameters by van't Hoff and Eyring analyses, respectively. The equilibrium data ($\Delta H^\circ_{\text{exp}} = 10.9 \pm 0.7$ kcal·mol^{−1}, $\Delta S^\circ_{\text{exp}} = 24.8 \pm 1.8$ cal·mol^{−1}·K^{−1}; $\Delta G^\circ_{\text{exp}} = +3.6$ kcal·mol^{−1}) show that endothermic N₂ splitting is entropically driven at higher temperatures. Furthermore, the forward activation parameters ($\Delta H^\ddagger_{\text{exp}} = 30.1 \pm 0.9$ kcal·mol^{−1}; $\Delta S^\ddagger_{\text{exp}} = +2.3 \pm 0.4$ cal·mol^{−1}·K^{−1}; $\Delta G^\ddagger_{298} = 29.4$ kcal·mol^{−1}) confirm a prohibitively high kinetic barrier for either direction at room temperature. An almost identical entropy of activation was reported for the cleavage of complex **A** ($\Delta H^\ddagger_{\text{exp}} = 23.3 \pm 0.3$ kcal·mol^{−1}; $\Delta S^\ddagger_{\text{exp}} = +2.3 \pm 1.1$ cal·mol^{−1}·K^{−1}), which proceeds via the zigzag transition state described above. Nishibayashi and co-workers previously reported the photolytic splitting of an N₂ bridged complex and reverse N–N coupling upon oxidation of the resulting molecular nitride.¹⁸ However, the thermal interconversion of **3** and **4** represents the first example of fully reversible N₂ splitting and nitride coupling, without the addition of external redox reagents.

Thermal N₂ splitting was examined computationally by DFT (Scheme 2), corroborating the equilibrium found for the N–N splitting reaction ($\Delta G^\circ_{\text{DFT}} = -0.7$ kcal·mol^{−1}). Notably, the computed minimum structure of the nitride product resembles the pincer conformation of dimer **3'** with increased pyramidalization of the PNP nitrogen atom in comparison to **3**. The higher stability of this conformation in **4** is attributed to competing π -donation of the amide and nitride ligands. The transition state (TS) for splitting of complex **3** is found at considerably lower energy on the singlet than on the triplet surface (¹TS $\Delta H^\ddagger_{\text{calc},S} = 37.6$ kcal·mol^{−1}, $\nu_{\text{img}} = -357$ cm^{−1}; ³TS $\Delta H^\ddagger_{\text{calc},T} = 59.1$ kcal·mol^{−1}, $\nu_{\text{img}} = -161$ cm^{−1}). Closer agreement with experiment is obtained for the activation barrier of the singlet conformer **3'** (¹TS' $\Delta H^\ddagger_{\text{calc},S} = 33.6$ kcal·mol^{−1}, $\nu_{\text{img}} = -368$ cm^{−1}), suggesting facile conformational rearrangement of the pincer backbone with negligible kinetic impact on route to the singlet transition state. All TS structures exhibit zigzag distorted $\{\text{WNNW}\}$ cores with evolving W–N multiple bond character as indicated by bond shortening (³ d_{DFT} 1.885 Å; ¹TS 1.753 Å; ³TS 1.752 Å; ³ d'_{DFT} 1.931 Å; ¹TS' 1.755 Å). A considerably smaller degree of distortion

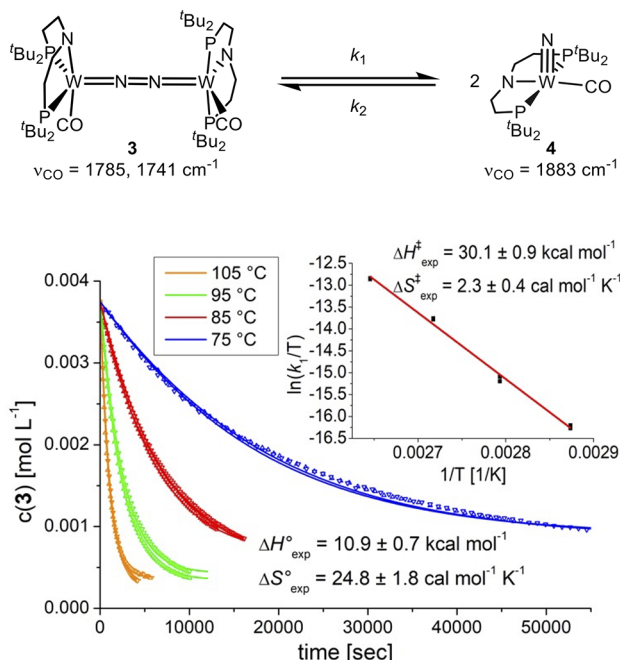


Figure 4. Concentration vs time plot for the thermal dissociation of **3** at different temperatures. The solid lines represent the results from fitting to the kinetic model. (inset) Eyring plot for the conversion of **3** into **4** ($R^2 = 0.995$).

from the ground state geometry is required on the singlet surface, as expressed by the shorter N–N distance (^1TS 1.809 Å, $^1\text{TS}'$ 1.789 Å vs ^3TS 1.981 Å) and smaller W–N–N angle (^1TS 151° , $^1\text{TS}'$ 152° vs ^3TS 160°), which is in line with the lower kinetic barrier. The preference for the characteristic in plane zigzag ^1TS reflects previous computational studies for systems that undergo N–N cleavage or reverse nitride coupling, such as $\{\pi^{10}\}$ complex **A** (^1TS $d_{\text{MoN}} = 1.760$ Å, $d_{\text{NN}} = 1.623$ Å, $\theta_{\text{MoNN}} = 148^\circ$), the computational model complex $[\text{N}_2\{\text{W}(\text{NH}_2)_3\}_2]$ (^1TS $d_{\text{WN}} = 1.781$ Å, $d_{\text{NN}} = 1.458$ Å, $\theta_{\text{WNN}} = 145^\circ$), or $[(\text{N}_2)\{\text{WCl}(\text{HPNP})\}_2]^{2+}$ (^1TS $d_{\text{WN}} = 1.764/1.740$ Å, $d_{\text{NN}} = 1.598$ Å, $\theta_{\text{WNN}} = 140.67^\circ/153.54^\circ$), respectively.^{31,57,61,62}

More details with respect to the relevant spin-state energetics were obtained from a relaxed surface scan along the N–N bond, considering the two pincer conformations that start from **3** and **3'** in their singlet and triplet electronic configurations (Figure 5). At no point along the scan, a clear

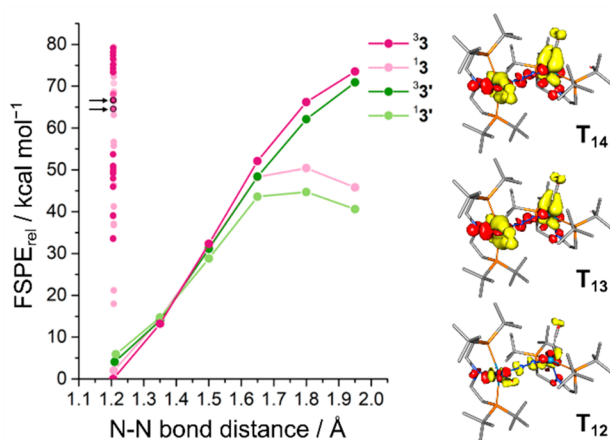


Figure 5. (left) Relaxed surface scan for **3** and **3'** in their singlet and triplet states, respectively. Excited states in the ground state geometry of **3** as predicted with TD-DFT are shown as smaller circles and the states T_{12} and $\text{T}_{13}/\text{T}_{14}$ in the Franck–Condon region are marked with black arrows. (right) Difference densities (yellow density loss, red density gain, contour value 0.003) of the excited states T_{12} , T_{13} , and T_{14} .

open-shell singlet (OSS) state could be identified; the Mulliken spin populations on the tungsten ions remain below ± 0.25 for a putative OSS in any of the available geometries. At N–N distances between 1.35–1.50 Å, the singlet and triplet states are essentially degenerate, while above 1.65 Å the singlet states of each conformer are energetically favored with $^1\text{3}'$ forming the lowest-lying surface. In comparison, for N_2 bridged Mo triamide platforms, the singlet and triplet state surfaces were computed to cross at larger separations (ca. 1.5–1.6 Å).^{67,63}

In comparison with our structurally and electronically related $\{\pi^{10}\delta^4\}$ complex $[(\text{N}_2)\{\text{ReCl}(\text{PNP})\}_2]$ (**D**; $\Delta H^\circ_{\text{DFT}} = 26.0$ kcal·mol⁻¹; $\Delta H^\circ_{\text{exp}} = +24 \pm 1$ kcal·mol⁻¹), thermal cleavage of **3** exhibits less favorable thermochemistry and kinetics.³⁰ The simplified electronic structure considerations for N–N splitting discussed above (Figure 2) imply a reorganization of the $^3\{\text{WNNW}\}$ core that leads to transfer of two electrons from the ground-state $\pi^*-\pi-\pi^*$ MO to the $\sigma-\sigma^*-\sigma$ originating MO and crossing onto the dissociative $^1\{\text{W}\equiv\text{N} + \text{N}\equiv\text{W}\}$ surface. The thermochemistry and kinetics

should therefore correlate with the relative energies of these MOs along the reaction coordinate. From this picture, some qualitative predictions can be derived upon replacing a weak π -donor ligand (**D**) for the strong π -acceptor CO, which mixes with the π -MO manifold. Depletion of electron density from the metal by backdonation to CO should thermodynamically disfavor N–N splitting, which is reductive in nature, as evidenced by the CO stretching vibrations of **3** and **4** (see above). Furthermore, stabilization of both $\pi^*-\pi-\pi^*$ MOs in the C_2 symmetric dicarbonyl dimer is expected to raise the overall barrier for N–N scission. We therefore attribute the less favorable thermochemistry and higher kinetic barriers for N–N cleavage of **3** vs **D** at least in part to the presence of the CO ligands.

Photodissociation of N_2

The photodriven splitting of related Re pincer platforms was recently reported by the groups of Schneider (**B**, Figure 1) and Miller (**C**) and was therefore also examined for **3**.^{20,22} While thermal dissociation at room temperature is both thermochemically and kinetically unfavorable, quantitative N–N splitting is obtained within 8 h upon photolysis in benzene at $\lambda = 427$ nm (LED, $\Delta\lambda = 10$ nm). As for complex **B**, a low quantum yield below 1% ($\Phi_{427\text{ nm}} = 0.37 \pm 0.03\%$) was obtained. The quantum yield shows no significant temperature dependence over a wide range (-80 to 25°C), suggesting that conformational equilibria of the ground state have no effect on the photochemical process. Broadband irradiation with a Xe-arc lamp ($\lambda = 395$ – 590 nm) around the strong absorption band at 511 nm (Figure 6) gave similar results. Photolysis with

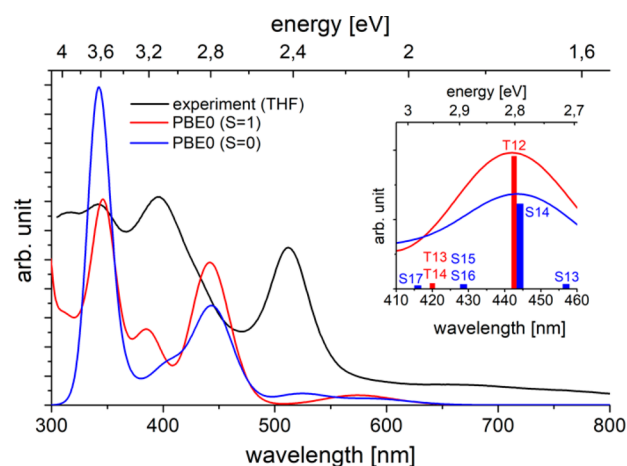


Figure 6. Experimental (black) and TD-DFT-computed (blue $S = 0$; red $S = 1$; see the SI for details) electronic absorption spectra. (inset) Computed productive region for N_2 cleavage.

wavelengths >540 nm resulted in significantly reduced photocleavage rates and no conversion was obtained above $\lambda > 590$ nm. On the other hand, shorter wavelengths ($\lambda < 395$ nm) gave substantial amounts of undefined side products. Competing N–N vs M– N_2 photodissociation was observed for some other N_2 bridged group six complexes.^{15,16,22} However, photolysis of **3** at $\lambda > 305$ nm under $^{15}\text{N}_2$ does not lead to ^{15}N incorporation into the nitride photoproduct, suggesting that the W– N_2 bond is photostable under these conditions. Photolysis of **4** at $\lambda > 305$ nm also showed decomposition of the nitride into undefined products. The

photodegradation at low wavelengths might be attributed to CO dissociation from **3** and/or **4**.

The density and nature of accessible electronic states upon photoexcitation were examined computationally with TD-DFT. The computed electronic absorption spectra for **3** and **13** are blue-shifted by ca. 0.38 eV with respect to the experimental spectrum (Figure 6). **3** shows best agreement with the experimental intensity distribution and relative energies (see the SI). However, **13** exhibits excitations of almost identical character in the spectral region that is relevant for the photoreactivity (see Figure 6 and the SI). The intense band in the visible range ($E_{\text{exp}} = 2.4$ eV (511 nm)) overlaps with the low energy edge of the photochemically productive region (~ 550 nm). It is assigned to transition T_{12} (**3** $E_{\text{calc}} = 2.8$ eV (443 nm)) as an excitation within the {WNNW} π manifold that shifts electron density from the N_2 -bridge to the metal ions (Figure 5). At slightly higher energy, two transitions of low intensity (T_{13} , T_{14} ; $E_{\text{calc}} = 2.89$ eV) involve excitations from the δ -type orbitals with significant CO contributions into $\pi^*-\pi^*-\pi^*$ MOs that are delocalized over the {WNNW} core. Both types of states therefore mainly exhibit charge transfer character within the core, either predominantly N_2 -to-W (T_{12}) or W-to- N_2 (T_{13}/T_{14}), respectively. Additional CT character to the pincer nitrogen atom is more pronounced in T_{13}/T_{14} than in T_{12} .

A high density of states around and below the photochemically relevant excited states T_{12} and T_{13}/T_{14} was found. In these states, orbitals of predominant $\pi^*-\pi-\pi^*$ and $\pi^*-\pi^*-\pi^*$ character are partially occupied (see the SI). The system may therefore evolve in the FC region to SOC-coupled singlet and triplet states with excitation character of initially δ to $\pi^*-\pi^*-\pi^*$ or δ to $\pi^*-\pi-\pi^*$ type. However, derivation of energy gradients by TD-DFT excited-state relaxation was not successful. Furthermore, TD-DFT cannot describe homolytic bond cleavage at large displacement from the equilibrium geometry beyond the Coulson–Fischer point^{64–69} and does not capture double excitations, which are expected to become increasingly relevant closer to the dissociation limit. Note that within the simple MO considerations (Figure 2), the **14** product surface can be considered a doubly excited state of **13**. Theoretical description of the excited state dynamics therefore requires more refined treatment, which is impeded by the currently available computational methodologies and resources for a complex as large as **3**.

Spectroscopic Examination of N_2 Photodissociation

The photochemistry of **3** was examined by ultrafast UVvis/UVvis and UVvis/IR transient absorption spectroscopies in THF. Different pump wavelengths in the productive range (400, 440, 475, 511, 530 nm) were applied, all giving similar observations (Figure 7 and the SI). Directly after excitation, the transient difference spectra show bleaching in the centers and enhanced absorption at the low energy sides of the ground state absorption spectrum. This is a clear signature of a vibrationally hot electronic ground state molecule being formed within the temporal resolution of the experiment ($\tau_{\text{exc}} \approx 70 \pm 20$ fs), as no features of an electronically excited state were found. Experiments using 330 and 380 nm pump wavelengths confirmed slow decomposition into undefined products, corroborating the results from steady state photolysis.

Thermal cooling results in almost full relaxation at times >60 ps, which is consistent with the low quantum yield for N–N

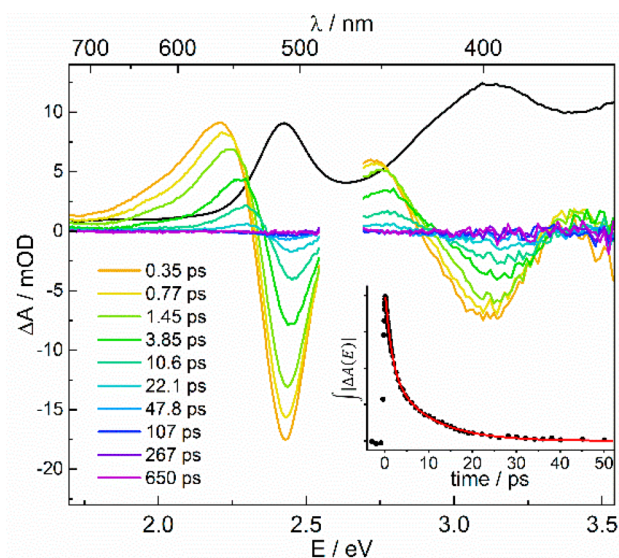


Figure 7. Transient UV/vis difference spectra of **3** in THF at selected pump–probe delays (pump wavelength 475 nm). The black line shows the scaled linear absorption spectrum. (inset) Time-dependence of the integrated absolute absorption changes (the red line is a biexponential fit).

bond cleavage. The relaxation dynamics of the ground state were quantified by analyzing the integral over the absolute value of the UVvis/UVvis difference spectra $|\Delta A(E)|$ over the whole measured spectral range (inset in Figure 7). Its time dependence was fitted by a biexponential decay giving time constants (relative amplitudes) of $\tau_1 = 1.5 \pm 0.2$ ps (54%) and $\tau_2 = 9.2 \pm 0.5$ ps (46%), respectively. The 9.2 ps component is a typical value for the vibrational energy transfer time of a highly excited molecule in a solvent. The fast component hints at a nonstatistical energy distribution created by preferential population of those vibrational modes, which couple to the electronic transition. The time scale of $\tau_1 = 1.5$ ps is consistent with intramolecular vibrational redistribution (IVR) to establish a quasi-equilibrium of the internal energy.^{70–75} This assignment is supported by the observation that the amplitudes of the hot bands depend on the pump wavelength (see the SI). UV-pump (400 nm) mid-IR-probe spectroscopy using the strong CO stretching modes as spectroscopic probes also indicate fast internal conversion (IC) followed by cooling dynamics in the ground state (see the SI). Here, recovery of the ground state bleach of the CO absorption band occurs with a characteristic time of 16 ± 3 ps.

The transient spectroscopy data is in agreement with two conceivable pathways for the photoreactivity of **3**, i.e., (a) nonradiative electronic electron/hole recombination within temporal resolution followed by N–N dissociation of the vibrationally hot ground state or (b) ultrafast internal conversion from the Franck–Condon (FC) region onto the dissociative singlet surface. The experimental derivation of the ground-state kinetic barrier ($\Delta H_{\text{exp}}^\ddagger = 30.1 \pm 0.9$ kcal·mol^{−1}; $\Delta S_{\text{exp}}^\ddagger = +2.3 \pm 0.4$ cal·mol^{−1}·K^{−1}) allowed for estimating whether the photon energy is sufficient for a vibrationally hot and internally equilibrated ground state to dissociate within the time scale of thermal cooling in the solvent bath. Using the ground-state frequency computations obtained from DFT, an upper limit for the internal temperature was estimated ($T_{\text{exc}} \approx 500$ K) that arises from excitation with a 400 nm photon,

followed by ultrafast internal conversion (IC) to the ground-state and IVR mediated vibrational equilibration (see the SI). Importantly, at that temperature the unimolecular rate for N–N dissociation ($k_{500\text{ K}} = 2.3\text{ s}^{-1}$) cannot compete with the rapid cooling rate ($\tau_2 \approx 9.2\text{ ps}$).

In consequence, photoreactivity from a hot ground state requires nonstatistical vibrational energy distribution, which rapidly decays with the time scale of IVR ($\tau_1 = 1.5\text{ ps}$). Thus, productive vibrational modes might be activated directly upon excitation. We therefore turned to resonance Raman (rR) spectroscopy, which exhibits a signal enhancement, if a dipole allowed electronic transition is coupled to a vibrational mode that is totally symmetric for the ground and excited state geometries and aligns with the displacement of the potential energy surface upon excitation.⁷⁶ The low symmetry of **3** in the ground state (C_2) should be beneficial to allocate the fundamental modes of the {WNNW} core that are coupled to the strong absorption band at 511 nm, which marks the low energy edge of the photochemically productive spectral window. rR spectra ($\lambda_{\text{exc}} = 514.5\text{ nm}$) of **3** and the isotopologue $^{15}\text{N}_2\text{-3}$ showed distinct differences for three bands: Besides the N–N stretching mode (ν_{NN}), the maximum of a broad feature at 491 cm^{-1} is red-shifted by around -12 cm^{-1} for $^{15}\text{N}_2\text{-3}$ (Figure 8). Furthermore, the weak band at 692 cm^{-1}

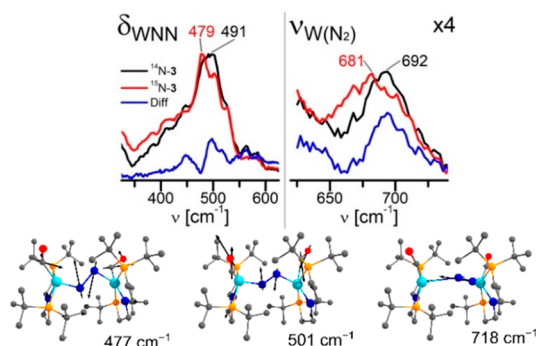


Figure 8. (top) Expansions of the rR spectra ($\lambda_{\text{exc}} = 514.5\text{ nm}$; $-50\text{ }^{\circ}\text{C}$) of **3** (black) and $^{15}\text{N}_2\text{-3}$ (red) and difference spectrum for the two isotopologues (blue) with band assignments (the right spectrum is scaled by a factor of 4). (bottom) Computed bending modes of the {WNNW} core of **3**.

cm^{-1} exhibits an isotope shift of -11 cm^{-1} . These features lie within the range for deformation (δ_{MNN}) and stretching (ν_{MN}) modes of terminal and linearly bridged N_2 complexes.^{77–81} The assignment of the isotope sensitive rR bands are supported by DFT computations. Below 500 cm^{-1} , two modes that represent a zigzag-type distortion of the {WNNW} core were found ($\delta_{\text{WNN}}^{\text{DFT}} = 475\text{ cm}^{-1}$, 477 cm^{-1} ; Figure 8) with isotopic shifts of $\Delta\delta_{\text{WNN}}^{\text{DFT}} = -8$ and -6 cm^{-1} , respectively. The weaker band is assigned to a W– N_2 stretching mode ($\nu_{\text{MN}}^{\text{DFT}} = 718\text{ cm}^{-1}$; $\Delta\nu_{\text{MN}}^{\text{DFT}} = -19\text{ cm}^{-1}$). The rR data therefore support the coupling of bending modes of the {WNNW} core, which reflect the ground-state reaction coordinate, with excitation(s) in the photochemically productive region.

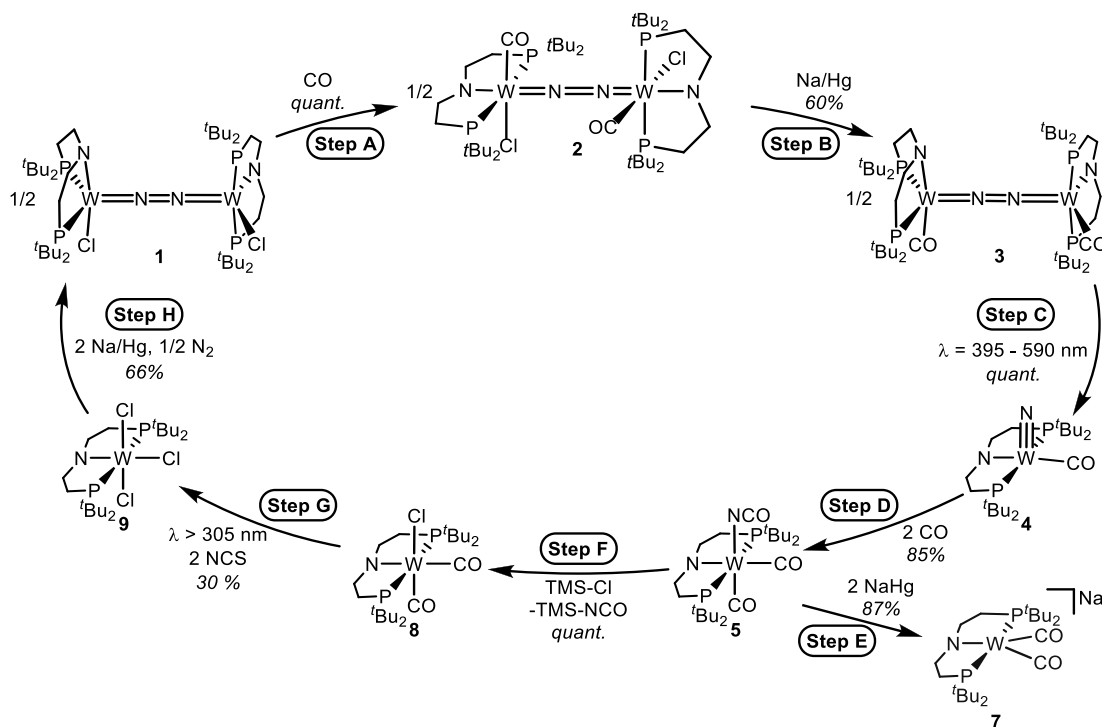
Nitride Carbonylation and Transfer

Terminal nitride complexes that were reported from thermal N_2 splitting are generally weak nucleophiles often requiring strong electrophiles for functionalization. The endothermic nature of the N_2 splitting reaction might lead to more activated

nitrides and facilitate nitrogen transfer reactivity. This was evaluated by isocyanate formation. Besides C–N coupling of N_2 complexes with CO,⁹ only one example for initial N_2 splitting and subsequent nitride carbonylation is currently known.⁸² Reaction of **4** with CO (1 atm) gives deep purple $[\text{W}(\text{NCO})(\text{CO})_2(\text{PNP})]$ (**5**) in yields up to 85% (Scheme 3, Step D). In the IR spectrum of **5**, the intense band at $\nu_{\text{NCO}} = 2203\text{ cm}^{-1}$ ($\Delta\nu_{15\text{N}} = 6\text{ cm}^{-1}$) and two CO stretching modes ($\nu_{\text{CO}} = 1909, 1832\text{ cm}^{-1}$) evidence the formation of the dicarbonyl isocyanate complex. The ^{15}NCO isotopologue was obtained from isotopically labeled $^{15}\text{N-4}$, confirming N_2 as nitrogen source. The ^{15}N NMR signal of $^{15}\text{NCO-5}$ ($\delta_{\text{N}} = -347\text{ ppm}$; $^2J_{\text{NP}} = 2.6\text{ Hz}$) is flanked by tungsten satellites, corroborating N-coordination of the cyanate-ligand. The *cis*-dicarbonyl configuration of **5** was further confirmed by X-ray crystallography (Figure 9, top).

Two pathways for isocyanate formation are conceivable, i.e., (a) direct, outer-sphere attack of CO at the nitrogen atom, in reversion of the related N_2 elimination reaction from coordinated azide or (b) a stepwise mechanism with initial coordination of CO to the metal and subsequent transfer to the nitride ligand. Inter- vs intramolecular C–N bond formation was distinguished by a ^{13}CO labeling experiment. Reaction of **4** with ^{13}CO selectively yields $[\text{W}(\text{NCO})-(^{13}\text{CO})_2(\text{PNP})]$ ($(^{13}\text{CO})_2\text{-5}$), as evidenced by IR and ^{13}C NMR spectroscopy (Figure 10). Analogous results were obtained upon reaction of **4** with isocyanides (CNR, R = ^tBu , $\text{C}_6\text{H}_4\text{-OMe}$; Figure 10) with no indication for carbodiimide isomers. Both the labeling experiment and the reaction with isocyanide therefore confirm intramolecular attack at the nitride ligand as the favored pathway for heterocumulene formation.

Cyanate release was examined on two different routes. Reduction of **5** with Na/Hg (2 equiv) yields bright orange $\text{Na}[\text{W}(\text{CO})_2(\text{PNP})]$ (**7**; Scheme 3, Step E) in isolated yields up to 87%. The tungstate(0) product **7** exhibits square pyramidal ($\tau_5 = 0.15$)⁴⁴ coordination in the solid state with an apical CO ligand (Figure 9, middle). A single ^{13}C NMR CO signal ($\delta_{\text{C}} = 240\text{ ppm}$) and one ^tBu ^1H NMR resonance ($\delta_{\text{H}} = 1.32\text{ ppm}$) indicate averaged C_{2v} symmetry on the NMR time scale. Strong backbonding is evidenced by low CO stretching frequencies ($\nu_{\text{CO}} = 1677, 1604\text{ cm}^{-1}$). Alternatively, cyanate release is enabled by salt-metathesis with Me_3SiCl . $[\text{WCl}(\text{CO})_2(\text{PNP})]$ (**8**) and Me_3SiNCO are obtained in almost quantitative spectroscopic yields, respectively (Scheme 3, Step F). The chloro complex **8** features similar spectroscopic and structural properties as parent **5** (Figure 9, bottom). Me_3SiNCO can be easily separated from the reaction mixture by *trap-to-trap* transfer of the solvent and was identified spectroscopically by comparison with an authentic sample. Silylisocyanate generation from N_2 was finally confirmed by ^{15}N labeling. The full synthetic cycle for the conversion of N_2 into trimethylsilylisocyanate could finally be closed by oxidation of **8** with *N*-chlorosuccinimide (NCS, 2 equiv.) under photolytic conditions ($\lambda > 305\text{ nm}$). The tungsten(IV) trichloride $[\text{WCl}_3(\text{PNP})]$ (**9**) was obtained in yields up to 30% (Scheme 3, Step G). Irradiation is required to obtain complete decarbonylation. Complex **9** is the direct precursor to the N_2 complex **1** (Scheme 3, Step H).³¹

Scheme 3. Synthetic Cycle for Photodriven Formation of Me_3SiNCO from N_2 and CO^a ^aNCS = N-chlorosuccinimide.

DISCUSSION

The thermal dissociation of linearly N_2 bridged ditungsten complex **3** into terminal nitride complex **4** is a unique example of fully reversible N_2 cleavage. The reaction is endothermic and entropically driven at elevated temperatures. As for Cummins' complex **A** (Figure 1), a similarly small entropy of activation was found. Computational analysis confirmed an analogous zigzag distortion of the $\{\pi^{10}\delta^4\}$ $^3\{\text{WNNW}\}$ core when approaching the transition state, which is located on the singlet surface. This displacement lifts the quasi-degenerate MOs of the $\{\text{WNNW}\}$ π -manifold and stabilizes the vacant $\sigma-\sigma^*-\sigma$ MO. Reduction of the symmetry by bending leads to mixing of σ/π MOs, which lowers the energy for intersystem crossing of the ^3A starting and ^1A product states and ultimately the kinetic barrier for N_2 dissociation. Our DFT results reflect the analysis for oxygen atom transfer from $\text{R}_3\text{P}=\text{O}$ to $\text{M}(\text{OSiR})_3$ ($\text{M} = \text{V}, \text{Nb}, \text{Ta}$) by Wolczanski and Cundari as well as Cummins' qualitative bonding model for N_2 splitting (Figure 2).^{2,83} Along these lines, we associate the endothermic nature of $\text{N}-\text{N}$ scission with the presence of the strongly π -accepting carbonyl ligands, which compete with the N_2 bridge for back-bonding from the metal ions. These considerations similarly apply to the kinetic barrier, which should be increased by π -accepting ligands that stabilize the $\pi^*-\pi-\pi^*$ donor level of the ground state (Figure 11). In fact, **3** is the first carbonyl dinitrogen complex that was reported to undergo N_2 splitting.

The presence of the CO ligands allows for estimating the degree of the net tungsten to nitrogen electron transfer that is associated with $\text{N}-\text{N}$ cleavage. This is by no means obvious. Significant covalent contributions to metal bonding with the nitride ligand are expected,⁸⁴⁻⁸⁶ as was shown for various terminal nitride complexes, e.g. by electronic and EPR spectroscopy and computational bond analysis.^{28,55,87,88}

Bendix et al. therefore proposed the use of the Enemark–Feltham notation for nitride complexes to avoid ambiguities from formal oxidation states which lose their physical meaning with increasing covalency.^{39,40} Similarly, Holland pointed out for N_2 complexes that the broad range of $\text{N}-\text{N}$ stretching vibrations exhibits a decent agreement with Badger's rule, indicating a continuum of electron transfer that arises from covalent contributions to $\text{M}-\text{N}_2$ bonding and backbonding.^{3,4,89} In the current case, $\text{N}-\text{N}$ cleavage results in a distinct blue-shift of the CO stretching vibration by more than 100 cm^{-1} . For comparison, the 1-electron oxidation of monocarbonyl complex $\text{trans}[\text{ReCl}(\text{CO})(\text{Ph}_2\text{PCH}_2\text{CH}_2\text{PPh}_2)_2]$ is associated with a smaller blueshift of 74 cm^{-1} ,⁹⁰ suggesting that the electronic and structural reorganization associated with $\text{N}-\text{N}$ cleavage is accompanied by considerable net M -to- N electron transfer.

A limited number of mechanistic studies reported computed thermochemical and kinetic parameters for the splitting of $\mu^2-\eta^1:\eta^1-\text{N}_2$ bridged complexes into terminal nitrides.^{2,7,20,21,29-31,35,36,91} In some cases, experimental kinetic data was obtained and generally showed good agreement of the kinetic barrier (ΔG^\ddagger) within about $5\text{ kcal}\cdot\text{mol}^{-1}$. As all of these systems were computed to proceed through the distinct zigzag transition state, a scaling relationship for the reaction free energies and free energies of activation should arise, if the electronic rearrangement within the $\{\text{MNNM}\}$ core determines the thermochemistry and kinetics of $\text{N}-\text{N}$ splitting. In fact, the computational data for the reported $4d/5d$ platforms that cover a variety of metals, ligands, redox and spin states, and coordination geometries exhibit a surprisingly good agreement with a simple Marcus-type quadratic free energy relationship ($\Delta G^\ddagger = (\lambda + \Delta G^\circ)^2/4\lambda$) using the reorganization energy λ as a single parameter (Figure 12).^{4,92} The correlation

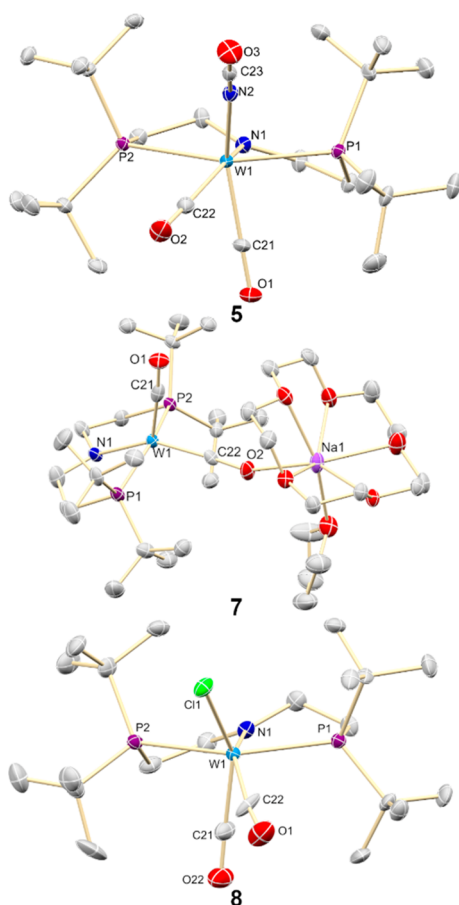


Figure 9. Molecular structures of **5**, **7**, and **8** in the crystal from X-ray diffraction. Hydrogen atoms were omitted for clarity. Selected bond lengths [Å] and angles [°] for **5** [W1–N1 2.011(3), W1–C21 1.964(4), W1–C22 2.028(4), W1–P1 2.5077(10), W1–P2 2.5030(10), W–N2 2.116(3); C21–W1–N1 153.31(14), C22–W1–N1 85.54(15), C21–W1–C22 77.03(16), P1–W1–P2 155.09(3), C21–W1–N2 146.74(15)], **7** [W1–N1 2.088(6), W1–C21 1.902(9), W1–C22 1.911(8), W1–P1 2.426(2), W1–P2 2.4484(19); C21–W1–N1 148.0(3), C22–W1–N1 124.3(3), C21–W1–C22 87.7(3), P1–W1–P2 156.74(6)], and **8** [W1–N1 2.013(6), W1–C21 1.939(8), W1–C22 2.056(8), W1–P1 2.5175(19), W1–P2 2.516(2), W1–Cl1 2.4682(19); C21–W1–N1 152.9(3), C22–W1–N1 89.2(3), C21–W1–C22 73.0(3), P1–W1–P2 155.24(6), C21–W1–Cl1 143.0(3)].

supports that the reaction energetics are dominated by the electronic reorganization through the common, zigzag transition state (Figure 2), while other factors like sterics are less relevant. The current study allows for the first time experimental benchmarking of both kinetic and thermochemical computational parameters with satisfying results. The computed value fits well with the previous data for $\lambda = 160$ kcal·mol^{−1} (Figure 12). This high reorganization energy suggests that accessible kinetic barriers require driving forces around or below $\Delta G^\circ = -20$ kcal·mol^{−1} for thermal dissociation of $\mu^2\text{-}\eta^1\text{-}\eta^1\text{-N}_2$ bridged complexes. In consequence, the resulting terminal nitride complexes are easily over-stabilized hampering subsequent functionalization or even catalytic turnover. Photochemically driven N–N scission is therefore an interesting strategy to break this unfavorable scaling relation and even benefit from kinetically inaccessible barriers for the reverse process, i.e. bimolecular nitride coupling.

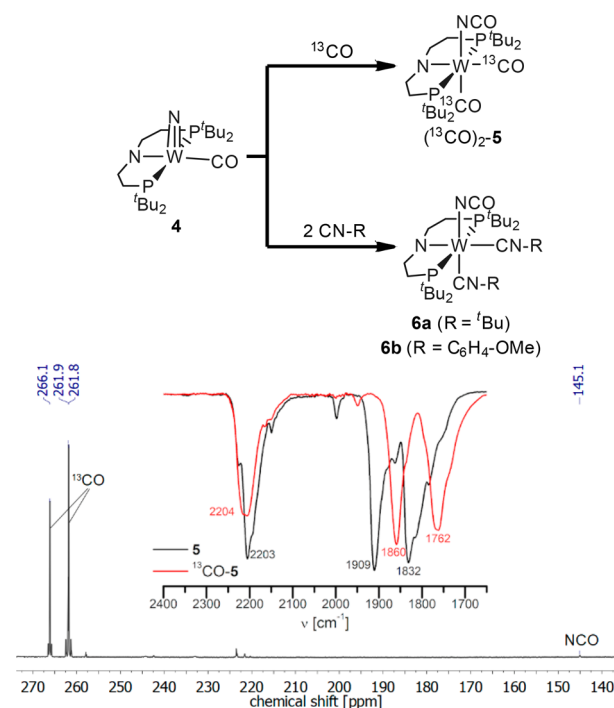


Figure 10. (top) Reactions of nitride complex **4** with ^{13}CO and isocyanides. (bottom) $^{13}\text{C}\{^1\text{H}\}$ NMR spectrum of $(^{13}\text{CO})_2\text{-5}$ and IR spectra of **5** (black) and $(^{13}\text{CO})_2\text{-5}$ (red).

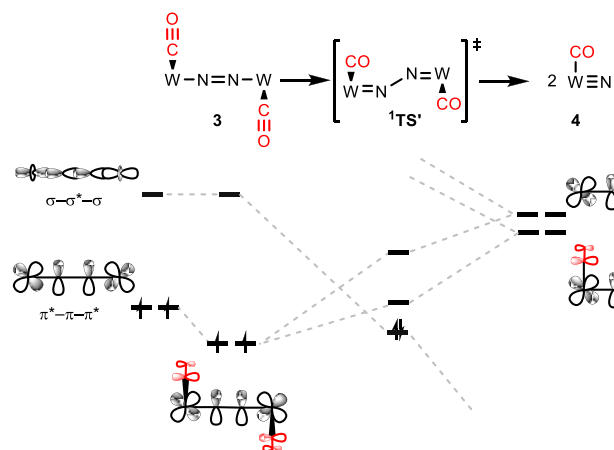


Figure 11. Qualitative MO correlation diagram with relevant interactions for the splitting of **3** into **4**.

Photolysis of **3** in the range $\lambda = 395\text{--}590$ nm quantitatively produces nitride **4** at room temperature. UVvis/UVvis and UVvis/IR pump–probe spectroscopy revealed ultrafast excited state decay within the temporal resolution of the optical probe experiment ($\tau_{\text{exc}} \approx 70 \pm 20$ fs). Rapid nonradiative excited state decay is in line with the high computed density of states in the FC region and below according to the “energy gap law”.^{93,94} In comparison, the photostable complex $[(\mu^2\text{-}\eta^1\text{-}\eta^1\text{-N}_2)\{\text{Mo}(\text{PPh}_2\text{Me})_2(\text{PhTpy})\}_2]^{2+}$ (PhTpy = 4'-Ph-2,2',6',2''-terpyridine) exhibits much slower recovery of the electronic ground state within 15–25 ps.²³ This π^{10} -complex displays a similar degree of N_2 activation ($\nu_{\text{NN}} = 1563$ cm^{−1}) as **3** ($\nu_{\text{NN}} = 1598$ cm^{−1}), yet with a $^1\text{A}_g$ ground state that originates from splitting of the $\pi^*-\pi-\pi^*$ MOs in D_{2h} symmetry.⁹⁵ In contrast to **3**, excitations in the vis/NIR region were assigned to

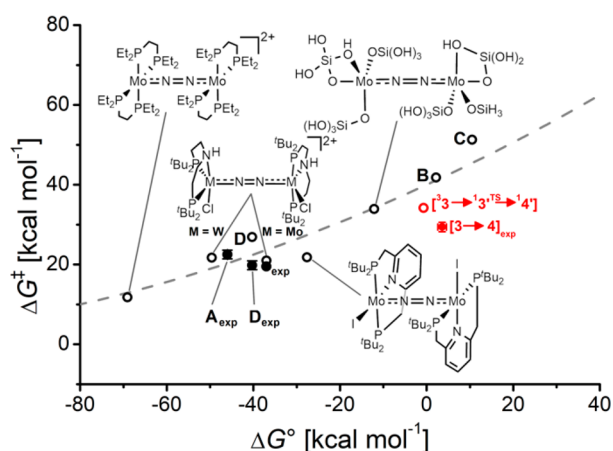


Figure 12. Correlation of reaction free energies and free energies of activation for the splitting of $\mu^2\text{-}\eta^1\text{:}\eta^1\text{-N}_2$ bridged complexes into terminal nitrides (open circles $\Delta G^\ddagger_{\text{DFT}}(\Delta G^\circ_{\text{DFT}})$; closed circles $\Delta G^\ddagger_{\text{exp}}(\Delta G^\circ_{\text{DFT}})$ and $\Delta G^\ddagger_{\text{exp}}(\Delta G^\circ_{\text{exp}})$ for 3). The dashed line denotes a Marcus model ($\Delta G^\ddagger = (\lambda + \Delta G^\circ)/2/4\lambda$) for $\lambda = 160 \text{ kcal}\cdot\text{mol}^{-1}$ [Adapted with permission from ref 4. Copyright 2021 American Chemical Society].

$^1\text{MLCT}$ transitions to the Tpy auxiliary ligands. Relaxation kinetics were attributed to rapid intersystem crossing (ISC) and decay via a cascade of $^3\text{MLCT}$ states as main channel, which shifts electron density back to the {MoNNMo} core. Notably, TD-DFT modeling of the $^1\text{MLCT}$ excited state indicate preserved linearity of the core. In consequence, the ν_{NN} stretching mode, which exhibits a Fermi resonance with the Tpy chromophore, is the only rR active mode that is $^{14/15}\text{N}_2$ sensitive.²⁴ It is tempting to associate the lack of N–N photodissociation of this complex with a lack of bending modes that are activated by electronic excitation and prepare a vibrationally excited core that passes through the zigzag TS in the electronic ground state.

This notion is supported by results from Blank and Cummins for the photochemically active complex A (Figure 1).²² Dissociation proceeds upon excitation (540 nm) to a triplet state with $(\pi\text{-}\pi^*\text{-}\pi)^3(\pi^*\text{-}\pi\text{-}\pi^*)^3$ character, which reflects the nature of the intense transition T_{12} of 3 (Figure 6). Based on simple orbital considerations, this is remarkable, as this transition should weaken M–N and strengthen N–N bonding relative to the triplet $(\pi\text{-}\pi^*\text{-}\pi)^4(\pi^*\text{-}\pi\text{-}\pi^*)^2$ ground state. However, as in the case of 3, subps electron–hole recombination was observed and N–N dissociation was attributed to vibrationally excited ground-state reactivity. An oscillation in the pump–probe decay (70 cm^{-1}) was associated with an activated low energy {MoNNMo} bending mode. Further support for nonstatistical vibrational energy distribution came from different N–N over Mo–N dissociation yields for the photochemical and thermal routes, respectively.

Our comparison of the cooling kinetics of 3 with thermal dissociation rates emphasizes that a vibrationally equilibrated ground state cannot dissociate within the time scale of cooling in the solvent bath. Nonstatistical vibrational energy distribution would therefore be a prerequisite for hot ground state reactivity, reflecting Blank's and Cummins' results. It is plausible that the accessible CT states within the core, such as T_{12} , experience some degree of distortion with respect to the near linear ground-state geometry. McNaughton et al. presented a detailed analysis of vibronic coupling in

$[\text{Mo}^{\text{III}}(\text{N}_2)(\text{N}_3\text{N})]$.⁹⁶ Its ^2E ground state configuration (i.e., $(\pi\text{-}\pi^*)^3$ applying the notation used in Figure 2 to this mononuclear complex with an end-on N_2 ligand) is pseudo-Jahn–Teller coupled to bending modes that are perpendicular to the Mo–N–N axis. The rR data of complex 3 indicate that stretching and bending modes of the {WNNW} core are activated upon excitation in the productive optical region. To this end, our results are in line with a scenario, in which vibronically coupled modes that align with the zigzag reaction coordinate facilitate quasi-thermal N–N photodissociation on the ground state surface (Figure 13, blue path). Besides A,

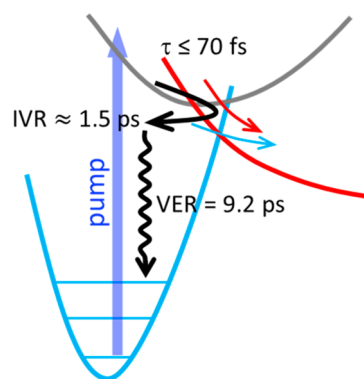


Figure 13. Schematic sketch of the conceivable paths for photo-dissociation of 3 via a vibrationally excited ground state (black/blue path) or excited state crossing onto the dissociative product surface (red path).

such a path was also observed for N_2 photoelimination from a ferric azide complex.⁹⁷ Computational examinations of thermal N_2 elimination from azide complexes feature related $[\text{M}=\text{N}\cdots\text{N}=\text{N}]$ zigzag transition states.^{55,98} Notably, dissociative chemisorption of N_2 on heterogeneous ruthenium catalysts was recently shown to be facilitated by plasma-induced vibrational excitation of N_2 .^{99,100}

We need to emphasize that the ultrafast electronic relaxation of 3 and low quantum yield did not allow for excluding a path that leads from the FC region to the photoproduct without repopulation of the ^3A ground state (Figure 13, red path). We note in passing that the excited states T_{13}/T_{14} resemble our assignments for the productive excitations of photoactive complex B (Figure 1), while the analogous transition of T_{12} was in that case outside the suitable energy window.²⁰ However, our simple Marcus analysis (Figure 12) suggests that in the ground state geometry of 3 the dissociative ^1A potential energy surface should be at high energy ($\lambda = 160 \text{ kcal}\cdot\text{mol}^{-1}$), implying large structural reorganization to enable surface crossing. Detailed theoretical analysis of the excited state dynamics with consideration of vibronic interactions and competing SOC requires the use of multideterminantal methods, which is currently impeded by the large size of the system.

The enhanced reactivity of the photolytically produced nitride was demonstrated by near quantitative nitride carbonylation at ambient conditions. Isocyanate formation from nitride complexes and CO was previously reported in several instances,^{101–109} yet only for one example coupled to N_2 splitting.⁸⁸ In that case, selective carbonylation of the N_2 splitting product required oxidation from $\text{V}^{\text{IV}}/\text{V}^{\text{IV}}$ to $\text{V}^{\text{V}}/\text{V}^{\text{V}}$. In a complementary approach, Sita and co-workers reported the coupling of an N_2 derived terminal imido ligand with CO,

giving free Me_3ENCO ($\text{E} = \text{C}, \text{Si}, \text{Ge}$).¹⁹ Given this precedence, nitride carbonylation is mechanistically surprisingly ill-defined regarding direct CO attack at the nitride vs intramolecular coupling of coordinated CO. A computational study by Liddle and co-workers supported CO coordination to azide-derived U^{V} and U^{VI} nitrides, prior to C–N bond formation.¹¹³ Such an inner-sphere pathway was also proposed for CO oxygenation by terminal oxo complexes and the microscopic reverse oxidative addition of CO_2 .^{110–112} ^{13}C labeling of nitride **4** experimentally confirmed intramolecular CO attack at the nitride ligand, which is in agreement with Liddle's findings. It is reasonable to assume that C–N coupling is triggered by initial coordination of CO at the five-coordinate nitride complex. The strong π -acceptor ligand in *trans*-position should enhance the electrophilicity of the nitride ligand and facilitate reaction with ambiphilic CO.

The synthetic cycle for isocyanate formation from N_2 and CO (Scheme 3) also demonstrates the limitations of this system. The dicarbonyl complex **8** that is obtained after isocyanate release does not directly undergo reductive N_2 activation but requires full oxidative decarbonylation under photolytic conditions, which comes with moderate yields. Future work will therefore target heterocumulene formation without deactivation by additional CO.

EXPERIMENTAL SECTION

Materials and Synthetic Methods

All experiments were carried out under inert conditions using standard Schlenk and glovebox techniques (argon atmosphere). All solvents were purchased in HPLC quality (Sigma-Aldrich) and dried using an MBRAUN Solvent Purification System. THF, HMDSO, and toluene were additionally dried over an Na/K-alloy. Deuterated solvents were obtained from Eurisotop GmbH and dried over an Na/K-alloy (C_6D_6 , THF- d_8 , Tol- d_8), distilled by trap-to-trap transfer *in vacuo* and degassed by three freeze–pump–thaw cycles, respectively. Silica gel 60 silanized was purchased from Merck KGaA and heated at 120 °C *in vacuo* for 5 days prior to use. Purification of CO gas (Air Liquide) was obtained by passing the gas through a steel coil cooled to –78 °C. ^{13}C O (Eurisotop GmbH, 99.30%) and $^{15}\text{N}_2$ (Sigma-Aldrich, 98% ^{15}N) were used without further purification. *N*-Chlorosuccinimide (NCS) was sublimed prior to use. Me_3SiNCO and Me_3SiCl were distilled and degassed. *t*-Butylisocyanide (Sigma-Aldrich) and 4-methoxyphenylisocyanide (Sigma-Aldrich) were used as purchased without further purification, whereas $[(\text{N}_2)\{\text{WCl}(\text{PNP})\}_2]$ (**1**) was synthesized according to published procedures.³¹

Analytical Methods

NMR spectra were recorded on Bruker Avance III 300 or Avance III 400 spectrometers or an Avance 500 spectrometer with a Prodigy broadband cryoprobe, respectively, and calibrated to the residual solvent signals (C_6D_6 $\delta_{\text{H}} = 7.16$ ppm, $\delta_{\text{C}} = 128.4$ ppm; THF- d_8 $\delta_{\text{H}} = 3.58$ ppm, $\delta_{\text{C}} = 67.6$ ppm, Tol- d_8 $\delta_{\text{H}} = 2.09$ ppm, $\delta_{\text{C}} = 20.4$ ppm). ^{31}P and ^{15}N NMR chemical shifts are reported relative to external phosphoric acid and nitromethane ($\delta = 0.0$ ppm), respectively. Signal multiplicities are abbreviated as s (singlet), d (doublet), m (multiplet), br (broad).

Elemental analyses were obtained from the Analytisches Labor, Georg-August-Universität (Göttingen, Germany) using an Elementar Vario EL 3 analyzer. LIFDI-MS (linden cms) spectra were measured by the Zentrale Massenabteilung, Fakultät für Chemie, Georg-August-Universität Göttingen. Resonance Raman spectra for **2** and **3** were recorded using a HORIBA Scientific LabRAM HR 800 spectrometer with open-electrode CCD detector in combination with a free space optical microscope and a He:Ne-laser (632.8 nm). Additionally, Raman spectra for **3** were recorded using a Triple Raman Spectrometer TR 557 from S&I (Spectroscopy & Imaging GmbH).

IR spectra were recorded using a Bruker ALPHA FT-IR spectrometer with Platinum ATR module.

Magnetic moments in solution were determined by Evans' method as modified by Sur and corrected for diamagnetic contribution.^{113,114} Magnetic susceptibility measurements in the solid state were carried out with a Quantum Design MPMS-XL-5 SQUID magnetometer in the temperature range from 295 to 2 K at 0.5 T applied field. The powdered sample was contained in a Teflon bucket and fixed in a nonmagnetic sample holder. Each raw data point for the measured magnetic moment of the sample was corrected for the diamagnetic contribution by subtraction of the experimentally determined magnetic measurement of the Teflon bucket. The molar susceptibility data were corrected for the diamagnetic contribution using the Pascal constants and the increment method according to Haberditzel.^{115,116} Experimental data were modeled with the *JulX* program.¹¹⁷ UVvis spectra were recorded on an Agilent Cary 60 equipped with an Unisoku Cryostat (CoolSpek) and magnetic stirrer using quartz cuvettes with an attached tube and a J-Young-cap. All UVvis samples were prepared in a glovebox and transferred out of the glovebox prior to the measurement.

Synthesis

$[(\text{N}_2)\{\text{WCl}(\text{CO})(\text{PNP})\}_2]$ (**2**). $[(\text{N}_2)\{\text{WCl}(\text{PNP})\}_2]$ (**1**) (100 mg, 84 μmol) is dissolved in benzene (10 mL), degassed via two freeze–pump–thaw cycles and stirred under CO (1 atm) for 20 min. After removal of volatiles *in vacuo*, **2** is obtained as a black-yellow solid in quantitative yield. Longer reaction times lead to loss of N_2 and formation of $[\text{WCl}(\text{CO})_2(\text{PNP})]$ (**8**). Crystals suitable for X-ray diffraction were obtained by cooling a saturated Et_2O solution to –40 °C. The synthesis of ^{15}N -**2** was carried out starting from $[(^{15}\text{N}_2)\{\text{WCl}(\text{PNP})\}_2]$.

$^1\text{H}\{^{31}\text{P}\}$ NMR (C_6D_6 , 500 MHz, [ppm]): $\delta = 3.55$ (m, 4 H, NCHH), 3.26 (m, 4 H, NCHH), 2.42 (m, 4 H, PCHH), 1.89 (m, 4 H, PCHH), 1.60 (s, 18 H, CMe_3), 1.53 (s, 18 H, CMe_3), 1.43 (s, 18 H, CMe_3), 1.31 (s, 18 H, CMe_3). $^{13}\text{C}\{^1\text{H}\}$ NMR (C_6D_6 , 126 MHz, [ppm]): $\delta = 25.4$ (AXY, $N = |^1J_{\text{AX}} + ^3J_{\text{AY}}| = 16.9$ Hz, 2x PCH_2), 25.7 (AXY, $N = |^1J_{\text{AX}} + ^3J_{\text{AY}}| = 17.1$ Hz, 2x PCH_2), 31.0 (m, 2x CMe_3), 31.1 (m, 2x CMe_3), 31.3 (m, 2x CMe_3), 31.4 (m, 2x CMe_3), 37.2 (AXY, $N = |^1J_{\text{AX}} + ^3J_{\text{AY}}| = 16.0$ Hz, 2x PCMe_3), 37.8 (AXY, $N = |^1J_{\text{AX}} + ^3J_{\text{AY}}| = 16.7$ Hz, 2x PCMe_3), 38.4 (AXY, $N = |^1J_{\text{AX}} + ^3J_{\text{AY}}| = 10.5$ Hz, 2x PCMe_3), 38.8 (AXY, $N = |^1J_{\text{AX}} + ^3J_{\text{AY}}| = 11.5$ Hz, 2x PCMe_3), 59.2 (AXY, $N = |^2J_{\text{AX}} + ^4J_{\text{AY}}| = 9.9$ Hz, 2x NCH_2), 59.4 (AXY, $N = |^2J_{\text{AX}} + ^4J_{\text{AY}}| = 9.6$ Hz, 2x NCH_2), 263 (m, 2x CO). $^{15}\text{N}\{^1\text{H}\}$ NMR (THF- d_8 , 50.7 MHz, [ppm]): $\delta = -0.69$ (s). $^{31}\text{P}\{^1\text{H}\}$ NMR (THF- d_8 , 162 MHz, [ppm]): $\delta = 65.9$ (s). **Elem. Anal.** found (calc) for $\text{C}_{42}\text{H}_{88}\text{Cl}_2\text{N}_4\text{O}_2\text{P}_4\text{W}_2$: C 40.63 (40.56); H 6.69 (7.13); N 4.52 (4.51). **IR** (ATR-IR, cm^{-1}): 1883 (ν_{CO}); 1867 (ν_{CO}). **rRaman** ($\lambda_{\text{ex}} = 457$ nm, frozen THF- d_8 , $[\text{cm}^{-1}]$): ^{14}N -21437 (ν_{NN}); ^{15}N -2 1394 (ν_{NN}).

$[(\text{N}_2)\{\text{W}(\text{CO})(\text{PNP})\}_2]$ (**3**). Complex **2** (80 mg, 67 μmol , 1.0 equiv) and Na/Hg (2.2 g, 162 μmol , 2.4 equiv) are stirred for 12 h in benzene (20 mL) under the exclusion of light. After removal of the solvent *in vacuo*, the residue is extracted over *celite* with pentane to give **3** as a red-brown solid (45 mg, 57%). Crystals suitable for X-ray diffraction were obtained by layering a saturated THF solution with HMDSO. ^{15}N -**3** was synthesized starting from ^{15}N -**2**.

$^1\text{H}\{^{31}\text{P}\}$ NMR (C_6D_6 , 300 MHz, [ppm]): $\delta = 14.6$ (s, CHH), 13.6 (s, CHH), 12.9 (s, CHH), 7.79 (s, CHH), 7.25 (s, 'Bu), 6.45 (s, CHH), 6.38 (s, 'Bu), 4.54 (s, 'Bu), 3.53 (s, 'Bu), –2.58 (s, CHH), –14.4 (s, CHH), –16.0 (s, CHH). **Elem. Anal.** found (calc) for $\text{C}_{42}\text{H}_{88}\text{N}_4\text{O}_2\text{P}_4\text{W}_2$: C 43.17 (43.01), H 7.23 (7.56), N 3.64 (4.78). (The lower N content found is attributed to partial N_2 loss during combustion analysis.) **IR** (ATR-IR, cm^{-1}): 1785 (ν_{CO}); 1741 (ν_{CO}). $\mu_{\text{eff}} = 2.4 \pm 0.1 \mu_{\text{B}}$. **rRaman** ($\lambda_{\text{ex}} = 633$ nm, frozen THF- d_8 , $[\text{cm}^{-1}]$): ^{14}N -3 1589 (ν_{NN}); ^{15}N -3 1540 (ν_{NN}). **rRaman** ($\lambda_{\text{ex}} = 514.5$ nm, THF- d_8 , –50 °C $[\text{cm}^{-1}]$): ^{14}N -3 1571 (ν_{NN}) 692 (ν_{WN}) 491 (δ_{WNN}); ^{15}N -3 1522 (ν_{NN}), 681 (ν_{WN}) 479 (δ_{WNN}).

$[\text{W}(\text{N})(\text{CO})(\text{PNP})]$ (**4**). (a) *Photolytic N_2 Splitting*. Complex **3** (10 mg, 8.53 μmol) is dissolved in C_6D_6 and photolyzed ($\lambda = 427$ nm, LED, $\Delta\lambda = 10$ nm) for 8 h in a water bath. The color changes from

deep red to pale blue. After evaporation of the solvent, **4** is obtained in quantitative yield. The synthesis of ^{15}N -**4** was carried out with ^{15}N -**3**.

(b) *Thermal N_2 Splitting*. Complex **3** (10 mg, 8.53 μmol) is dissolved in C_6D_6 and heated to 80 $^\circ\text{C}$ for 16 h with concomitant color change from deep red to pale blue.

$^1\text{H}\{^{31}\text{P}\}$ NMR (C_6D_6 , 500 MHz, [ppm]): δ = 3.90 (m, 2 H, NCHH), 3.76 (m, 2 H, NCHH), 1.79 (m, 2 H, PCHH), 1.55 (m, 2 H, PCHH), 1.49 (s, 18 H, 2x $\text{C}(\text{CH}_3)_3$), 0.89 (s, 18 H, 2x $\text{C}(\text{CH}_3)_3$). $^{13}\text{C}\{^1\text{H}\}$ NMR (C_6D_6 , 126 MHz, [ppm]): δ = 24.5 (AXY, $N = {}^1J_{\text{AX}} + {}^3J_{\text{AY}} = 18.5$ Hz, 2x PCH_2), 29.1 (AXY, $N = {}^1J_{\text{AX}} + {}^4J_{\text{AY}} = 5.4$ Hz, 2x $\text{C}(\text{CH}_3)_3$), 29.3 (AXY, $N = {}^1J_{\text{AX}} + {}^4J_{\text{AY}} = 5.5$ Hz, 2x $\text{C}(\text{CH}_3)_3$), 35.0 (AXY, $N = {}^1J_{\text{AX}} + {}^3J_{\text{AY}} = 15.5$ Hz, 2x $\text{C}(\text{CH}_3)_3$), 35.1 (AXY, $N = {}^1J_{\text{AX}} + {}^3J_{\text{AY}} = 20.5$ Hz, 2x $\text{C}(\text{CH}_3)_3$), 66.2 (AXY, $N = {}^1J_{\text{AX}} + {}^4J_{\text{AY}} = 14.8$ Hz, 2x NCH_2), 283.4 (t, ${}^2J_{\text{CP}} = 4.40$ Hz, CO). $^{15}\text{N}\{^1\text{H}\}$ NMR (C_6D_6 , 50.7 MHz, [ppm]): δ = 447.0 (s). $^{31}\text{P}\{^1\text{H}\}$ NMR (C_6D_6 , 203 MHz, [ppm]): δ = 104.4 (s). **Anal. found (calc)** for $\text{C}_{21}\text{H}_{44}\text{N}_2\text{O}_2\text{P}_2\text{W}$: C 43.03 (43.01), H 7.53 (7.56), N 4.93 (4.78). **IR (ATR-IR, cm^{-1})**: 1883 (ν_{CO}), 998 ($\nu_{\text{W}=\text{N}}$).

Coupling of Complex 4. Isolated **4** (5.2 mg, 8.87 μmol) was dissolved in toluene- d_8 , heated to 95 $^\circ\text{C}$ over 24 h under the exclusion of light and cooled to room temperature to freeze the equilibrium. ^1H NMR spectroscopy confirmed the selective conversion of about 10% of **4** to dinuclear **3**.

[W(NCO)(CO) $_2$ (PNP)] (5). Complex **4** (20 mg, 34.1 μmol) is dissolved in benzene. After degassing the solution by two freeze–pump–thaw cycles, the flask is backfilled with CO (1 atm) and solution stirred at room temperature. After 14 h, the solvent is removed *in vacuo* and the residue extracted through a plug of silanized silica 60. Evaporation of the solvent gives **5** as a deep purple solid (18.5 mg, 85%). The synthesis of ^{15}N -**5** was carried out with ^{15}N -**4**. Crystals suitable for X-ray diffraction were obtained by slow evaporation of a saturated Et_2O solution at -40 $^\circ\text{C}$.

$^1\text{H}\{^{31}\text{P}\}$ NMR (C_6D_6 , 500 MHz, [ppm]): δ = 1.02 (s, 18 H, 2x ^tBu), 1.21 (s, 18 H, 2x ^tBu), 1.76–1.88 (m, 4 H, 2x PCHH), 2.50–2.56 (m, 2 H, 2x PCHH), 2.95–3.01 (m, 2 H, 2x NCHH). $^{13}\text{C}\{^1\text{H}\}$ NMR (C_6D_6 , 126 MHz, [ppm]): δ = 26.9 (AXY, $N = {}^1J_{\text{AX}} + {}^3J_{\text{AY}} = 17.1$ Hz, 2x PCH_2), 29.8 (AXY, $N = {}^1J_{\text{AX}} + {}^4J_{\text{AY}} = 4.5$ Hz, 2x $\text{PC}(\text{CH}_3)_3$), 30.4 (AXY, $N = {}^1J_{\text{AX}} + {}^4J_{\text{AY}} = 3.9$ Hz, 2x $\text{PC}(\text{CH}_3)_3$), 37.3 (AXY, $N = {}^1J_{\text{AX}} + {}^3J_{\text{AY}} = 14.3$ Hz, 2x $\text{PC}(\text{CH}_3)_3$), 37.4 (AXY, $N = {}^1J_{\text{AX}} + {}^3J_{\text{AY}} = 14.3$ Hz, 2x $\text{PC}(\text{CH}_3)_3$), 68.2 (AXY, $N = {}^1J_{\text{AX}} + {}^4J_{\text{AY}} = 10.8$ Hz, 2x NCH_2), 145 (s_{br} , NCO), 261.8 (t, ${}^2J_{\text{CP}} = 8.3$ Hz, CO), 266.1 (t, ${}^2J_{\text{CP}} = 4.40$ Hz, CO). $^{15}\text{N}\{^1\text{H}\}$ NMR (C_6D_6 , 50.7 MHz, [ppm]): δ = -347 (t, ${}^2J_{\text{NP}} = 2.6$ Hz). $^{31}\text{P}\{^1\text{H}\}$ NMR (C_6D_6 , 162 MHz, [ppm]): δ = 76.6 (s). **Anal. found (calc)** for $\text{C}_{23}\text{H}_{44}\text{N}_2\text{O}_3\text{P}_2\text{W}$: 42.97 (43.00), H 6.82 (6.90), N 4.37 (4.36). **IR (ATR-IR, cm^{-1})**: 2205 (ν_{NCO}), 1910 (ν_{CO}), 1831 (ν_{CO}). **LIFDI-MS (m/z) found (calc)** for $[\text{C}_{23}\text{H}_{44}\text{N}_2\text{O}_3\text{P}_2\text{W}]$: 642.2 (642.2), 644.2 (644.2).

[W(NCO)(^{13}CO) $_2$ (PNP)] (^{13}CO -5**)**. Complex **4** (10.0 mg, 17.1 μmol) is dissolved in C_6D_6 . After degassing the solution by two freeze–pump–thaw cycles, the flask is backfilled with ^{13}CO (1 atm) and solution stirred at room temperature for 14 h. After removal of the solvent *in vacuo* the purple residue is extracted with Et_2O over a plug of silanized silica 60. Evaporation of the solvent gives ^{13}CO -**5** as a purple solid.

$^{13}\text{C}\{^1\text{H}\}$ NMR (C_6D_6 , 126 MHz, [ppm]): δ = 145 (s_{br} , NCO), 261.8 (dt, ${}^2J_{\text{CP}} = 8.5$ Hz, ${}^2J_{\text{CC}} = 8.5$ Hz, CO), 266.1 (dt, ${}^2J_{\text{CP}} = 4.40$ Hz, ${}^2J_{\text{CC}} = 9.0$ Hz, CO). $^{31}\text{P}\{^1\text{H}\}$ NMR (C_6D_6 , 162 MHz, [ppm]): δ = 76.6 (dd, ${}^2J_{\text{CP}} = 8.4$ Hz, ${}^2J_{\text{CP}} = 4.3$ Hz). **IR (ATR-IR, cm^{-1})**: 2205 (ν_{NCO}), 1860 ($\nu_{^{13}\text{CO}}$), 1762 ($\nu_{^{13}\text{CO}}$). **LIFDI-MS (m/z) found (calc)** for $[\text{C}_{21}^{13}\text{C}_2\text{H}_{44}\text{N}_2\text{O}_3\text{P}_2\text{W}]$: 644.2 (644.2), 646.2 (646.2).

[W(NCO)(CN ^tBu) $_2$ (PNP)] (6a**)**. CN ^tBu (7.8 μL , 5.7 mg, 69 μmol , 1.9 equiv) is added to a solution of **4** (21.3 mg, 36.3 μmol , 1.0 equiv) in benzene (20 mL). The mixture is heated to 85 $^\circ\text{C}$ for 3 h. After removal of the solvent *in vacuo*, the residue is extracted with benzene over silanized silica 60. After evaporation of the solvent, **6a** is obtained as a green solid (15.3 mg, 56%). Crystals suitable for X-ray diffraction were obtained by slow evaporation of a saturated Et_2O solution at -40 $^\circ\text{C}$.

$^1\text{H}\{^{31}\text{P}\}$ NMR (C_6D_6 , 300 MHz, [ppm]): δ = 3.10 (m, 2 H, NCHH), 2.76 (m, 2 H, NCHH), 1.99 (m, 2 H, PCHH), 1.90 (m, 2 H, PCHH), 1.46 (s, 9 H, CN-CMe $_3$), 1.39 (s, 18 H, 2x CMe $_3$), 1.27 (s, 18 H, 2x CMe $_3$), 1.11 (s, 9 H, CN-CMe $_3$). $^{13}\text{C}\{^1\text{H}\}$ NMR (C_6D_6 , 126 MHz, [ppm]): δ = 27.4 (AXY, $N = {}^1J_{\text{AX}} + {}^3J_{\text{AY}} = 14.0$ Hz, 2x PCH_2), 30.7 (s, 2x $\text{P}(\text{CMe}_3)_2$), 31.0 (s, 2x $\text{P}(\text{CMe}_3)_2$), 32.2 (s, CN-CMe $_3$), 32.3 (s, CN-CMe $_3$), 37.7 (AXY, $N = {}^1J_{\text{AX}} + {}^3J_{\text{AY}} = 11.8$ Hz, 2x $\text{P}(\text{CMe}_3)_2$), 39.0 (AXY, $N = {}^1J_{\text{AX}} + {}^3J_{\text{AY}} = 12.6$ Hz, 2x $\text{P}(\text{CMe}_3)_2$), 58.4 (s, CN-CMe $_3$), 63.6 (s, CN-CMe $_3$), 69.6 (AXY, $N = {}^1J_{\text{AX}} + {}^4J_{\text{AY}} = 12.1$ Hz, 2x NCH_2), 143 (s_{br} , NCO), 213 (s, CN- ^tBu), 246 (s, CN- ^tBu). $^{31}\text{P}\{^1\text{H}\}$ NMR (C_6D_6 , 121 MHz, [ppm]): δ = 76.6 (s). **Elem. Anal.** found (calc) for $\text{C}_{37}\text{H}_{58}\text{N}_4\text{O}_3\text{P}_2\text{W}$: C 49.65 (49.47), H 7.78 (7.80), N 7.00 (7.44). **IR (ATR-IR, cm^{-1})**: ν = 2203 (ν_{NCO}), 1994 ($\nu_{\text{C}=\text{N}}$), 1832 ($\nu_{\text{C}=\text{N}}$).

[W(NCO)(CNC $_6\text{H}_4\text{OMe}$) $_2$ (PNP)] (6b**)**. CNC $_6\text{H}_4\text{OMe}$ (4.5 mg, 34.1 μmol , 2.0 equiv) is added to a solution of **4** (10.0 mg, 17.1 μmol , 1.0 equiv) in benzene (5 mL). The mixture is heated to 85 $^\circ\text{C}$ for 3 h. After removal of the solvent *in vacuo*, the residue is extracted with benzene through silanized silica 60. After evaporation of the solvent, **6b** is obtained as a yellow-brownish solid (8.4 mg, 58%). Crystals suitable for X-ray diffraction were obtained by slow evaporation of a saturated Et_2O solution at -40 $^\circ\text{C}$.

$^1\text{H}\{^{31}\text{P}\}$ NMR (C_6D_6 , 300 MHz, [ppm]): δ = 7.33 (d, ${}^3J_{\text{HH}} = 8.99$ Hz, 2 H, Ar-H), 6.78 (d, ${}^3J_{\text{HH}} = 8.94$ Hz, 2 H, Ar-H), 6.75 (d, ${}^3J_{\text{HH}} = 8.91$ Hz, 2 H, Ar-H), 6.67 (d, ${}^3J_{\text{HH}} = 8.93$ Hz, 2 H, Ar-H), 3.31 (m, 2 H, NCHH), 3.23 (s, 3 H, OMe), 3.21 (s, 3 H, OMe), 2.84 (m, 2 H, NCHH), 2.01 (m, 4 H, PCHH), 1.37 (s, 18 H, 2x $\text{P}(\text{CMe}_3)_2$), 1.18 (s, 18 H, 2x $\text{P}(\text{CMe}_3)_2$). $^{13}\text{C}\{^1\text{H}\}$ NMR (C_6D_6 , 126 MHz, [ppm]): δ = 27.7 (AXY, $N = {}^1J_{\text{AX}} + {}^3J_{\text{AY}} = 15.6$ Hz, 2x PCH_2), 30.5 (AXY, $N = {}^1J_{\text{AX}} + {}^4J_{\text{AY}} = 5.21$ Hz, 2x $\text{P}(\text{CMe}_3)_2$), 30.8 (AXY, $N = {}^1J_{\text{AX}} + {}^4J_{\text{AY}} = 4.20$ Hz, 2x $\text{P}(\text{CMe}_3)_2$), 36.0 (AXY, $N = {}^1J_{\text{AX}} + {}^3J_{\text{AY}} = 13.8$ Hz, 2x $\text{P}(\text{CMe}_3)_2$), 37.8 (AXY, $N = {}^1J_{\text{AX}} + {}^3J_{\text{AY}} = 13.2$ Hz, 2x $\text{P}(\text{CMe}_3)_2$), 55.0 (s, O-Me), 69.6 (AXY, $N = {}^1J_{\text{AX}} + {}^4J_{\text{AY}} = 11.4$ Hz, 2x NCH_2), 115 (s, 2x ^{Ar}C), 114 (s, 2x ^{Ar}C), 122 (s, 2x ^{Ar}C), 124 (s, 2x ^{Ar}C), 135 (s_{br} , $^{Ar}\text{C}_q$), 136 (t, ${}^4J_{\text{CP}} = 2.47$ Hz, 2x $^{Ar}\text{C}_q$), 143 (s_{br} , NCO), 157 (s, $^{Ar}\text{C}_q$), 158 (s, $^{Ar}\text{C}_q$), 246 (s, CN-R), 257 (CN-R). $^{31}\text{P}\{^1\text{H}\}$ NMR (C_6D_6 , 121 MHz, [ppm]): δ = 78.7 (s). **Elem. Anal.** found (calc) for $\text{C}_{31}\text{H}_{62}\text{N}_4\text{O}_2\text{P}_2\text{W}$: C 52.37 (52.12), H 6.30 (6.86), N 6.20 (6.57). **IR (ATR-IR, cm^{-1})**: ν = 2205 (ν_{NCO}), 1911 ($\nu_{\text{C}=\text{N}}$), 1757 ($\nu_{\text{C}=\text{N}}$).

Na[W(CO) $_2$ (PNP)] (7**)**. Complex **5** (17.5 mg, 27.5 μmol , 1.0 equiv) and Na/Hg (823 mg, 60.5 μmol , 2.2 equiv) are stirred in THF for 4 h. The color changes from purple to bright orange. After filtration and evaporation of the solvent *in vacuo*, **5** is obtained as an orange solid (15 mg, 87%). After addition of 15-cr-5 (1.0 equiv), crystals suitable for X-ray diffraction were grown by diffusion of pentane into a saturated THF solution at -40 $^\circ\text{C}$.

$^1\text{H}\{^{31}\text{P}\}$ NMR (THF- d_8 , 500 MHz, [ppm]): δ = 3.22 (t, ${}^2J_{\text{HH}} = 6.42$ Hz, 4 H, NCH $_2$), 1.94 (t, ${}^2J_{\text{HH}} = 6.39$ Hz, 4 H, PCH $_2$), 1.32 (s, 36 H, 4x ^tBu). $^{13}\text{C}\{^1\text{H}\}$ NMR (THF- d_8 , 126 MHz, [ppm]): δ = 27.4 (AXY, $N = {}^1J_{\text{AX}} + {}^3J_{\text{AY}} = 10.8$ Hz, 2x PCH_2), 30.9 (AXY, $N = {}^1J_{\text{AX}} + {}^4J_{\text{AY}} = 6.3$ Hz, 4x $\text{P}(\text{CMe}_3)_2$), 38.5 (AXY, $N = {}^1J_{\text{AX}} + {}^3J_{\text{AY}} = 11.5$ Hz, 4x $\text{P}(\text{CMe}_3)_2$), 66.4 (AXY, $N = {}^1J_{\text{AX}} + {}^4J_{\text{AY}} = 19.7$ Hz, 2x NCH_2), 240 (s, 2x CO). $^{31}\text{P}\{^1\text{H}\}$ NMR (THF- d_8 , 121 MHz, [ppm]): δ = 105.4 (s). **Elem. Anal.** found (calc) for $\text{C}_{22}\text{H}_{44}\text{N}_4\text{NaO}_2\text{P}_2\text{W}$: C 42.35 (42.39), H 6.97 (7.11), N 2.21 (2.25). **IR (ATR-IR, cm^{-1})**: ν = 1677 (ν_{CO}), 1604 (ν_{CO}).

[WCl(CO) $_2$ (PNP)] (8**)**. Me $_3\text{SiCl}$ (1.0 μL , 0.9 mg, 7.8 μmol , 1.0 equiv) is added to a solution of **5** (5.0 mg, 7.8 μmol , 1.0 equiv) in THF- d_8 (0.5 mL). The solution is stirred overnight. **8** and Me $_3\text{SiNCO}$ are obtained as products in quantitative spectroscopic yield after separation by vacuum trap-to-trap transfer. Crystals suitable for X-ray diffraction were obtained by slow evaporation of a saturated Et_2O solution at -40 $^\circ\text{C}$.

$^1\text{H}\{^{31}\text{P}\}$ NMR (C_6D_6 , 300 MHz, [ppm]): 3.13–2.99 (m, 2 H, NCHH), 2.70–2.58 (m, 2 H, NCHH), 2.05–1.84 (m, 4 H, PCH $_2$), 1.34 (s, 18 H, CMe $_3$), 1.10 (s, 18 H, CMe $_3$). $^{13}\text{C}\{^1\text{H}\}$ NMR (C_6D_6 , 126 MHz, [ppm]): δ = 26.9 (AXY, $N = {}^1J_{\text{AX}} + {}^3J_{\text{AY}} = 17.1$ Hz, 2x PCH_2), 30.1 (AXY, $N = {}^1J_{\text{AX}} + {}^4J_{\text{AY}} = 4.6$ Hz, 2x $\text{PC}(\text{CH}_3)_3$), 31.0 (AXY, $N = {}^1J_{\text{AX}} + {}^4J_{\text{AY}} = 4.0$ Hz, 2x $\text{PC}(\text{CH}_3)_3$), 37.8 (AXY, $N = {}^1J_{\text{AX}} + {}^3J_{\text{AY}} = 13.6$ Hz, 2x $\text{PC}(\text{CH}_3)_3$), 38.5 (AXY, $N = {}^1J_{\text{AX}} + {}^3J_{\text{AY}} = 14.6$

Hz, 2x PC(CH₃)₃), 67.9 (AXY, $N = |^2J_{AX} + ^4J_{AKY}| = 11.0$ Hz, 2x NCH₂), 259 (t, $^2J_{CP} = 8.7$ Hz, CO), 264 (t, $^2J_{CP} = 4.8$ Hz, CO). ³¹P{¹H} NMR (C₆D₆, 162 MHz, [ppm]): δ = 73.9 (s). Anal. found (calc) C₂₂H₄₄ClNO₂P₂W: C 41.35 (41.56); H 7.00 (6.98); N 2.19 (2.20). IR (ATR-IR, cm⁻¹): 1914 (ν_{CO}), 1815 (ν_{CO}). (a) Characterization of TMS-NCO. ¹H NMR (THF-d₈, 300 MHz, [ppm]): δ = 0.25 (s, 9 H, Si(CH₃)₃). ¹³C{¹H} NMR (THF-d₈, 126 MHz, [ppm]): δ = 0.79 (s, 3 C, Si(CH₃)₃). ²⁹Si{¹H} NMR (THF-d₈, 90.4 MHz, [ppm]): δ = 4.5 (s). (b) Characterization of TMS-¹⁵NCO. ¹H NMR (THF-d₈, 500 MHz, [ppm]): δ = 0.25 (d, $^3J_{HN} = 1.4$ Hz, 9 H, Si(CH₃)₃). ¹³C{¹H} NMR (THF-d₈, 126 MHz, [ppm]): δ = 0.79 (d, $^2J_{CN} = 2.8$ Hz, 3 C, Si(CH₃)₃). ¹⁵N{¹H} NMR (THF-d₈, 50.7 MHz, [ppm]): δ = -346 (s). ²⁹Si{¹H} NMR (THF-d₈, 90.4 MHz, [ppm]): δ = 4.5 (d, $^1J_{SiN} = 14.2$ Hz).

Regeneration of [(WCl₃(PNP))]⁺ (9) from 8. Complex 8 (6.4 mg, 10.1 μmol, 1.0 equiv) and *N*-chlorosuccinimide (3.0 mg, 22.1 μmol, 2.2 equiv) are dissolved in C₆D₆ (0.5 mL) and photolyzed (λ > 305 nm) for 3 h. The color changes from deep purple to dark yellow and a dark precipitate forms. After removal of all volatiles *in vacuo* the residue is dissolved in a solution of C₆D₆ (0.5 mL) and 1,3,5-trimethoxybenzene as internal standard. 9 is obtained in 30% spectroscopic yield.

■ ASSOCIATED CONTENT

■ Supporting Information

The Supporting Information is available free of charge at <https://pubs.acs.org/doi/10.1021/jacsau.1c00117>.

Spectroscopic, kinetic, magnetic, crystallographic, and computational data (PDF, CIFs)

■ AUTHOR INFORMATION

Corresponding Authors

Vera Krewald – Theoretische Chemie, Technische Universität Darmstadt, 64287 Darmstadt, Germany; orcid.org/0000-0002-4749-4357; Email: krewald@chemie.tu-darmstadt.de

Dirk Schwarzer – Department of Dynamics at Surfaces, Max Planck Institute for Biophysical Chemistry, 37077 Göttingen, Germany; orcid.org/0000-0003-3838-2211; Email: dschwar@gwdg.de

Sven Schneider – University of Göttingen, Institute for Inorganic Chemistry, 37077 Göttingen, Germany; orcid.org/0000-0002-8432-7830; Email: sven.schneider@chemie.uni-goettingen.de

Authors

Bastian Schluschaß – University of Göttingen, Institute for Inorganic Chemistry, 37077 Göttingen, Germany

Jan-Hendrik Borter – Department of Dynamics at Surfaces, Max Planck Institute for Biophysical Chemistry, 37077 Göttingen, Germany

Severine Rupp – Theoretische Chemie, Technische Universität Darmstadt, 64287 Darmstadt, Germany

Serhiy Demeshko – University of Göttingen, Institute for Inorganic Chemistry, 37077 Göttingen, Germany

Christian Herwig – Institut für Chemie, Humboldt Universität zu Berlin, 12489 Berlin, Germany

Christian Limberg – Institut für Chemie, Humboldt Universität zu Berlin, 12489 Berlin, Germany; orcid.org/0000-0002-0751-1386

Nicholas A. Maciulis – Department of Chemistry, Indiana University, Bloomington, Indiana 47405-7102, United States

Jessica Schneider – University of Göttingen, Institute for Inorganic Chemistry, 37077 Göttingen, Germany

Christian Würtele – University of Göttingen, Institute for Inorganic Chemistry, 37077 Göttingen, Germany

Complete contact information is available at:

<https://pubs.acs.org/doi/10.1021/jacsau.1c00117>

■ Author Contributions

#J.-H.B. and S.R. contributed equally. B.S., N.A.M., and J.S. carried out the synthetic work, spectroscopic characterization, and the kinetic studies (B.S.), supervised by S.S. J.-H.B. performed the transient absorption spectroscopy, supervised by D.S., and S.R. performed the computational work under the supervision of V.K. S.D. carried out the magnetic characterization, and C.W. the crystallographic work. C.H. conducted the Raman experiments supervised by C.L. The paper was jointly written by B.S., J.-H.B., S.R., V.K., D.S., and S.S., and all authors discussed the results in detail, commented on the manuscript, and approved the final version.

■ Notes

The authors declare no competing financial interest.

■ ACKNOWLEDGMENTS

The authors thank Prof. K. C. Caulton for insightful discussion. This work was supported by the European Research Council (ERC Grant Agreement 646747), the German Research Foundation (grants: CRC1073/C07; SCHN950/7; KR4848/1), the Indiana University Office of Vice President for Research, and the U.S. National Science Foundation, Chemical Synthesis Program (SYN), by grant CHE-1362127. All calculations were conducted on the Lichtenberg high performance computer of TU Darmstadt. The Hessian Competence Center for High Performance Computing is gratefully acknowledged. The authors thank Dr. S. Dechert for recording resonance Raman spectra. Dr. S. Forrest and Dr. M. Otte are acknowledged with crystallographic data acquisition of 7 and 8, respectively.

■ REFERENCES

- (1) Laplaza, C. E.; Cummins, C. C. Dinitrogen Cleavage by a Three-Coordinate Molybdenum(III) Complex. *Science* **1995**, 268, 861–863.
- (2) Laplaza, C. E.; Johnson, M. J. A.; Peters, J. C.; Odom, A. L.; Kim, E.; Cummins, C. C.; George, G. N.; Pickering, I. J. Dinitrogen Cleavage by Three-Coordinate Molybdenum(III) Complexes: Mechanistic and Structural Data. *J. Am. Chem. Soc.* **1996**, 118, 8623–8638.
- (3) Klopsch, I.; Yuzik-Klimova, E.; Schneider, S. Functionalization of N₂ by Mid to Late Transition Metals via N–N Bond Cleavage. *Top. Organomet. Chem.* **2017**, 60, 71–112.
- (4) Forrest, S. J. K.; Schluschaß, B.; Yuzik-Klimova, E. Y.; Schneider, S. Nitrogen Fixation via Splitting into Nitrido Complexes. *Chem. Rev.* **2021**, DOI: [10.1021/acs.chemrev.0c00958](https://doi.org/10.1021/acs.chemrev.0c00958).
- (5) van der Ham, C. J. M.; Koper, M. T. M.; Hetterscheid, D. G. H. Challenges in reduction of dinitrogen by proton and electron transfer. *Chem. Soc. Rev.* **2014**, 43, 5183–5191.
- (6) Ertl, G. Surface Science and Catalysis-Studies on the Mechanism of Ammonia Synthesis: The P. H. Emmett Award Address. *Catal. Rev.: Sci. Eng.* **1980**, 21, 201–223.
- (7) Arashiba, K.; Eizawa, A.; Tanaka, H.; Nakajima, K.; Yoshizawa, K.; Nishibayashi, K. Catalytic Nitrogen Fixation via Direct Cleavage of Nitrogen-Nitrogen Triple Bond of Molecular Dinitrogen under Ambient Reaction Conditions. *Bull. Chem. Soc. Jpn.* **2017**, 90, 1111–1118.
- (8) Ashida, Y.; Arashiba, K.; Nakajima, K.; Nishibayashi, Y. Molybdenum-catalysed ammonia production with samarium diiodide and alcohols or water. *Nature* **2019**, 568, 536–540.

- (9) Kim, S.; Loose, F.; Chirik, P. J. Beyond Ammonia: Nitrogen-Element Bond Forming Reactions with Coordinated Dinitrogen. *Chem. Rev.* **2020**, *120*, 5637–5681.
- (10) Curley, J. J.; Sceats, E. L.; Cummins, C. C. A Cycle for Organic Nitrile Synthesis via Dinitrogen Cleavage. *J. Am. Chem. Soc.* **2006**, *128*, 14036–14037.
- (11) Klopsch, I.; Kinauer, M.; Finger, M.; Würtele, C.; Schneider, S. Conversion of Dinitrogen into Acetonitrile under Ambient Conditions. *Angew. Chem., Int. Ed.* **2016**, *55*, 4786–4789.
- (12) Guru, M.; Shima, T.; Hou, Z. Conversion of Dinitrogen to Nitriles at a Multinuclear Titanium Framework. *Angew. Chem., Int. Ed.* **2016**, *55*, 12316–12320.
- (13) Klopsch, I.; Schendzielorz, F.; Volkmann, C.; Würtele, C.; Schneider, S. Synthesis of Benzonitrile from Dinitrogen. *Z. Anorg. Allg. Chem.* **2018**, *644*, 916–919.
- (14) Krewald, V. Dinitrogen photoactivation: status quo and future perspectives. *Dalton Trans.* **2018**, *47*, 10320–10329.
- (15) Solari, E.; Da Silva, C.; Iacono, B.; Hesschenbrouck, J.; Rizzoli, C.; Scopelliti, R.; Floriani, C. Photochemical Activation of the N≡N Bond in a Dimolybdenum-Dinitrogen Complex: Formation of a Molybdenum Nitride. *Angew. Chem., Int. Ed.* **2001**, *40*, 3907–3909.
- (16) Curley, J. J.; Cook, T. R.; Reece, S. Y.; Müller, P.; Cummins, C. C. Shining Light on Dinitrogen Cleavage: Structural Features, Redox Chemistry, and Photochemistry of the Key Intermediate Bridging Dinitrogen. *J. Am. Chem. Soc.* **2008**, *130*, 9394–9405.
- (17) Kunkely, H.; Vogler, A. Photolysis of Aqueous $[(\text{NH}_3)_5\text{Os}(\mu\text{-N}_2)\text{Os}(\text{NH}_3)_5]^{5+}$: Cleavage of Dinitrogen by an Intramolecular Photoredox Reaction. *Angew. Chem., Int. Ed.* **2010**, *49*, 1591–1593.
- (18) Miyazaki, T.; Tanaka, H.; Tanabe, Y.; Yuki, M.; Nakajima, K.; Yoshizawa, K.; Nishibayashi, Y. Cleavage and Formation of Molecular Dinitrogen in a Single System Assisted by Molybdenum Complexes Bearing Ferrocenyldiphosphine. *Angew. Chem., Int. Ed.* **2014**, *53*, 11488–11492.
- (19) Keane, A. J.; Farrell, W. S.; Yonke, B.; Zavalij, P. Y.; Sita, L. R. Metal-Mediated Production of Isocyanates, $\text{R}_3\text{EN}=\text{C}=\text{O}$ from Dinitrogen, Carbon Dioxide, and R_3ECl . *Angew. Chem., Int. Ed.* **2015**, *54*, 10220–10224.
- (20) Schendzielorz, F.; Finger, M.; Abbenseth, J.; Würtele, C.; Krewald, V.; Schneider, S. Metal-Ligand Cooperative Synthesis of Benzonitrile by Electrochemical Reduction and Photolytic Splitting of Dinitrogen. *Angew. Chem., Int. Ed.* **2019**, *58*, 830–834.
- (21) Bruch, Q. J.; Connor, G. P.; Chen, C.-H.; Holland, P. L.; Mayer, J. M.; Hasanayn, F.; Miller, A. J. M. Dinitrogen Reduction to Ammonium at Rhenium Utilizing Light and Proton-Coupled Electron Transfer. *J. Am. Chem. Soc.* **2019**, *141*, 20198–20208.
- (22) Huss, A. S.; Curley, J. J.; Cummins, C. C.; Blank, D. A. Relaxation and Dissociation Following Photoexcitation of the $(\mu\text{-N}_2)[\text{Mo}(\text{N}[\text{t-BuAr}]_3)_2]$ Dinitrogen Cleavage Intermediate. *J. Phys. Chem. B* **2013**, *117*, 1429–1436.
- (23) Rafiq, S.; Bezdek, M. J.; Koch, M.; Chirik, P. J.; Scholes, G. D. Ultrafast Photophysics of a Dinitrogen-Bridged Molybdenum Complex. *J. Am. Chem. Soc.* **2018**, *140*, 6298–6307.
- (24) Rafiq, S.; Bezdek, M. J.; Chirik, P. J.; Scholes, G. D. Dinitrogen Coupling to a Terpyridine-Molybdenum Chromophore Is Switched on by Fermi Resonance. *Chem.* **2019**, *5*, 402–416.
- (25) Krewald, V.; González, L. A. A Valence-Delocalised Osmium Dimer capable of Dinitrogen Photocleavage: Ab Initio Insights into Its Electronic Structure. *Chem. - Eur. J.* **2018**, *24*, 5112–5123.
- (26) Krewald, V. Steric Switching From Photochemical to Thermal N₂ Splitting: A Computational Analysis of the Isomerization Reaction $\{(\text{Cp}^*)(\text{Am})\text{Mo}\}_2(\mu\text{-}\eta^1\text{-}\eta^1\text{-N}_2) \rightarrow \{(\text{Cp}^*)(\text{Am})\text{Mo}\}_2(\mu\text{-N})_2$. *Front. Chem.* **2019**, *7*, 352.
- (27) Rupp, S.; Plasser, F.; Krewald, V. Multi-Tier Electronic Structure Analysis of Sita's Mo and W Complexes Capable of Thermal or Photochemical N₂ Splitting. *Eur. J. Inorg. Chem.* **2020**, *2020*, 1506–1518.
- (28) Klopsch, I.; Finger, M.; Würtele, C.; Milde, B.; Werz, D. B.; Schneider, S. Dinitrogen Splitting and Functionalization in the Coordination Sphere of Rhenium. *J. Am. Chem. Soc.* **2014**, *136*, 6881–6883.
- (29) Silantyev, G.; Förster, M.; Schluschaß, B.; Abbenseth, J.; Würtele, C.; Volkmann, C.; Holthausen, M. C.; Schneider, S. Dinitrogen Splitting Coupled to Protonation. *Angew. Chem., Int. Ed.* **2017**, *56*, 5872–5876.
- (30) Lindley, B. M.; van Alten, R. S.; Finger, M.; Schendzielorz, F.; Würtele, C.; Miller, A. J. M.; Siewert, I.; Schneider, S. Mechanism of Chemical and Electrochemical N₂ Splitting by a Rhenium Pincer Complex. *J. Am. Chem. Soc.* **2018**, *140*, 7922–7935.
- (31) Schluschaß, B.; Abbenseth, J.; Demeshko, S.; Finger, M.; Franke, A.; Herwig, C.; Würtele, C.; Ivanovic-Burmazovic, I.; Limberg, C.; Telser, J.; Schneider, S. Selectivity of tungsten mediated dinitrogen splitting vs proton reduction. *Chem. Sci.* **2019**, *10*, 10275–10282.
- (32) Alten, R. S.; Watjen, F.; Demeshko, S.; Miller, A. J. M.; Würtele, C.; Siewert, I.; Schneider, S. (Electro-)chemical Splitting of Dinitrogen with a Rhenium Pincer Complex. *Eur. J. Inorg. Chem.* **2020**, *2020*, 1402–1410.
- (33) Hebden, T. J.; Schrock, R. R.; Takase, M. K.; Müller, P. Cleavage of dinitrogen to yield a (t-BuPOCOP)molybdenum(IV) nitride. *Chem. Commun.* **2012**, *48*, 1851–1853.
- (34) Liao, Q.; Cavaillé, A.; Saffon-Merceron, N.; Mézailles, N. Direct Synthesis of Silylamine from N₂ and a Silane: Mediated by a Tridentate Phosphine Molybdenum Fragment. *Angew. Chem., Int. Ed.* **2016**, *55*, 11212–11216.
- (35) Pucino, M.; Allouche, F.; Gordon, C. P.; Wörle, M.; Mougél, V.; Coperet, C. A reactive coordinatively saturated Mo(III) complex: exploiting the hemi-lability of tris(tert-butoxy)silanolate ligands. *Chem. Sci.* **2019**, *10*, 6362–6367.
- (36) Katayama, A.; Ohta, T.; Wasada-Tsutsui, Y.; Inomata, T.; Ozawa, T.; Ogura, T.; Masuda, H. Dinitrogen-Molybdenum Complex Induces Dinitrogen Cleavage by One-Electron Oxidation. *Angew. Chem., Int. Ed.* **2019**, *58*, 11279–11284.
- (37) Treitel, I. M.; Flood, M. T.; Marsh, R. E.; Gray, H. B. Molecular and electronic structure of μ -nitrogen-decaamminediruthenium(II). *J. Am. Chem. Soc.* **1969**, *91*, 6512–6513.
- (38) Chatt, J.; Fay, R. C.; Richards, R. L. Preparation and characterisation of the dinuclear dinitrogen complex, trichloro- μ -dinitrogen-bis(tetrahydrofuran){chlorotetrakis(dimethyl-(phenyl)-phosphine)rhenium(I)}chromium(III)[(PMe₂Ph)₄ClReN₂]. *J. Chem. Soc. A* **1971**, 702–704.
- (39) Bendix, J.; Meyer, K.; Weihermüller, T.; Bill, E.; Metzler-Nolte, N.; Wiegardt, K. Nitridocyanometalates of Cr^V, Mn^V, and Mn^{VI}. *Inorg. Chem.* **1998**, *37*, 1767–1775.
- (40) Scheibel, M. G.; Abbenseth, J.; Kinauer, M.; Heinemann, F. W.; Würtele, C.; de Bruin, B.; Schneider, S. Homolytic N-H Activation of Ammonia: Hydrogen Transfer of Parent Iridium Ammine, Amide, Imide, and Nitride Species. *Inorg. Chem.* **2015**, *54*, 9290–9302.
- (41) Bistoni, G.; Rampino, S.; Scafuri, N.; Ciancaleoni, G.; Zuccaccia, D.; Belpassi, L.; Tarantelli, F. How π back-donation quantitatively controls the CO stretching response in classical and non-classical metal carbonyl complexes. *Chem. Sci.* **2016**, *7*, 1174–1184.
- (42) Ariafard, A.; Brookes, N. J.; Stranger, R.; Yates, B. F. A. A Molecular Orbital Rationalization of Ligand Effects in N₂ Activation. *Chem. - Eur. J.* **2008**, *14*, 6119–6124.
- (43) The average N–N bond distance of **1** was used for comparison that originates from the two independent molecules in the asymmetric unit (1.33(4) and 1.27(8) Å).
- (44) Addison, A. W.; Rao, N. T.; Reedijk, J.; van Rijn, J.; Verschoor, G. C. Synthesis, structure, and spectroscopic properties of copper(II) compounds containing nitrogen-sulphur donor ligands; the crystal and molecular structure of aqua[1,7-bis(N-methylbenzimidazol-2'-yl)-2,6-dithiaheptane]copper(II) perchlorate. *J. Chem. Soc., Dalton Trans.* **1984**, 1349–1356.
- (45) Chatt, J.; Leigh, G. J.; Mingos, D. M. P. Configurations of some complexes of rhenium, ruthenium, osmium, rhodium, iridium, and

platinum halides with mono(tertiary phosphines) and mono(tertiary arsines). *J. Chem. Soc. A* **1969**, 1674–1680.

(46) Abbenseth, J.; Diefenbach, M.; Bete, S. C.; Würtele, C.; Volkmann, C.; Demeshko, S.; Holthausen, M. C.; Schneider, S. A square-planar osmium(II) complex. *Chem. Commun.* **2017**, 53, 5511–5514.

(47) Kinauer, M.; Diefenbach, M.; Bamberger, H.; Demeshko, S.; Reijerse, E. J.; Volkmann, C.; Würtele, C.; van Slagere, J.; de Bruin, B.; Holthausen, M. C.; Schneider, S. An iridium(III/IV/V) redox series featuring a terminal imido complex with triplet ground state. *Chem. Sci.* **2018**, 9, 4325–4332.

(48) Delony, D.; Kinauer, M.; Diefenbach, M.; Demeshko, S.; Würtele, C.; Holthausen, M. C.; Schneider, S. A Terminal Iridium Oxo Complex with a Triplet Ground State. *Angew. Chem., Int. Ed.* **2019**, 58, 10971–10974.

(49) Carreón-Macedo, J.-L.; Harvey, J. N. Do Spin states Matter in Organometallic Chemistry: A Computational Study. *J. Am. Chem. Soc.* **2004**, 126, 5789–5797.

(50) Carreón-Macedo, J.-L.; Harvey, J. N.; Poli, R. The Reductive Elimination of Methane from ansa-Hydrido(methyl)metallocenes of Molybdenum and Tungsten: Application of Hammond's Postulate to Two-State Reactions. *Eur. J. Inorg. Chem.* **2005**, 2005, 2999–3008.

(51) The carbonyl-stretching vibrations found for $^{15}\text{N-2}$ ($\nu_{\text{CO}} = 1887, 1867\text{ cm}^{-1}$), $^{15}\text{N-3}$ ($\nu_{\text{CO}} = 1785, 1745\text{ cm}^{-1}$), and $^{15}\text{N-4}$ ($\nu_{\text{CO}} = 1885\text{ cm}^{-1}$) are nearly identical compared to their ^{14}N -isotopologues (see the SI), indicating no coupling of the CO-stretching modes to the N—N or W≡N stretching modes, respectively.

(52) Dehnicke, K.; Strähle, J. The Transition Metal-Nitrogen Multiple Bond. *Angew. Chem., Int. Ed. Engl.* **1981**, 20, 413–426.

(53) Buhr, J. D.; Taube, H. Oxidation of pentaamminecarbonylosmium(2+) to mu.-dinitrogen-bis(cis-tetraamminecarbonylosmium)(4+). *Inorg. Chem.* **1979**, 18, 2208–2212.

(54) Che, C.; Lam, H.; Tong, W.; Lai, T.; Lau, T. Model reactions for nitrogen fixation. Photo-induced formation and X-ray crystal structure of $[\text{Os}_2(\text{NH}_3)_8(\text{MeCN})_2(\text{N}_2)]^{5+}$ from $[\text{Os}^{\text{VI}}(\text{NH}_3)_4\text{N}]^{3+}$. *J. Chem. Soc., Chem. Commun.* **1989**, 24, 1883–1884.

(55) Demadis, K. D.; Meyer, T. J.; White, P. S. Localization in trans-[(tpy)(Cl) $_{2\text{Os}}^{\text{III}}$ (N $_2$)Os $^{\text{II}}$ (Cl) $_2$ (tpy)] $^+$ (tpy = 2,2':6',2''-Terpyridine). *Inorg. Chem.* **1997**, 36, 5678–5679.

(56) Betley, T. A.; Peters, J. C. A Tetrahedrally Coordinated $\text{L}_3\text{Fe-N}_x$ Platform that Accommodates Terminal Nitride ($\text{Fe}^{\text{IV}}\equiv\text{N}$) and Dinitrogen ($\text{Fe}^{\text{I}}\text{-N}_2\text{-Fe}^{\text{I}}$) Ligands. *J. Am. Chem. Soc.* **2004**, 126, 6252–6254.

(57) Scheibel, M. G.; Askevold, B.; Heinemann, F. W.; Reijerse, E. J.; de Bruin, B.; Schneider, S. Closed-shell and open-shell square-planar iridium nitrido complexes. *Nat. Chem.* **2012**, 4, 552–558.

(58) Krahe, O.; Bill, E.; Neese, F. Decay of Iron(V) Nitride Complexes By a N-N Bond-Coupling Reaction in Solution: A Combined Spectroscopic and Theoretical Analysis. *Angew. Chem., Int. Ed.* **2014**, 53, 8727–8731.

(59) Abbenseth, J.; Finger, M.; Würtele, C.; Kananmascheff, M.; Schneider, S. Coupling of terminal iridium nitrido complexes. *Inorg. Chem. Front.* **2016**, 3, 469–477.

(60) Clarke, R. M.; Storr, T. Tuning Electronic Structure to Control Manganese Nitride Activation. *J. Am. Chem. Soc.* **2016**, 138, 15299–15302.

(61) Brookes, N. J.; Graham, D. C.; Christian, G.; Stranger, R.; Yates, B. F. The influence of peripheral ligand bulk on nitrogen activation by three-coordinate molybdenum complexes-A theoretical study using the ONIOM method. *J. Comput. Chem.* **2009**, 30, 2146–2156.

(62) Cui, Q.; Musaev, D. G.; Svensson, M.; Sieber, S.; Morokuma, K. N_2 Cleavage by Three-Coordinate Group 6 Complexes. W(III) Complexes Would Be Better Than Mo(III) Complexes. *J. Am. Chem. Soc.* **1995**, 117, 12366–12367.

(63) Christian, G.; Stranger, R.; Yates, B. F. A Comparison of N_2 Cleavage in Schrock's $\text{Mo}[\text{N}_3\text{N}]$ and Laplaza-Cummins' $\text{Mo}[\text{N}(\text{R})\text{-Ar}]_3$ Systems. *Chem. - Eur. J.* **2009**, 15, 646–655.

(64) Giesbertz, K. J. H.; Baerends, E. J. Failure of time-dependent density functional theory for excited state surfaces in case of homolytic bond dissociation. *Chem. Phys. Lett.* **2008**, 461, 338–342.

(65) Casida, M. E.; Huix-Rotllant, M. Progress in Time-Dependent Density-Functional Theory. *Annu. Rev. Phys. Chem.* **2012**, 63, 287–323.

(66) Coulson, C. A.; Fischer, I. Notes on the molecular orbital treatment of the hydrogen molecule. *Philos. Mag.* **1949**, 40, 386–393.

(67) Thompson, D. C.; Alavi, A. A comparison of Hartree-Fock and exact diagonalization solutions for a model two-electron system. *J. Chem. Phys.* **2005**, 122, 124107.

(68) Hait, D.; Rettig, A.; Head-Gordon, M. Well-behaved versus ill-behaved density functionals for single bond dissociation: Separating success from disaster functional by functional for stretched H_2 . *J. Chem. Phys.* **2019**, 150, 094115.

(69) Hait, D.; Rettig, A.; Head-Gordon, M. Beyond the Coulson-Fischer point: characterizing single excitation CI and TDDFT for excited states in single bond dissociations. *Phys. Chem. Chem. Phys.* **2019**, 21, 21761–21775.

(70) Schwarzer, D.; Hanisch, C.; Kutne, P.; Troe, J. Vibrational Energy Transfer in Highly Excited Bridged Azulene-Aryl Compounds: Direct Observation of Energy Flow through Aliphatic Chains and into the Solvent. *J. Phys. Chem. A* **2002**, 106, 8019–8028.

(71) Schwarzer, D.; Kutne, P.; Schröder, C.; Troe, J. Intramolecular vibrational energy redistribution in bridged azulene-anthracene compounds: ballistic energy transport through molecular chains. *J. Chem. Phys.* **2004**, 121, 1754–1764.

(72) Damrauer, N. H.; Cerullo, G.; Yeh, A.; Bousie, T. R.; Shank, C. V.; McCusker, J. K. Femtosecond Dynamics of Excited-State Evolution in $[\text{Ru}(\text{bpy})_3]^{2+}$. *Science* **1997**, 275, 54–57.

(73) Hedley, G. J.; Ruseckas, A.; Liu, Z.; Lo, S.-C.; Burn, P. L.; Samuel, I. D. W. Iridium metal complexes as an unambiguous probe of intramolecular vibrational redistribution. *J. Am. Chem. Soc.* **2008**, 130, 11842–11843.

(74) Delor, M.; Keane, T.; Scattergood, P. A.; Sazanovich, I. V.; Greetham, G. M.; Towrie, M.; Meijer, A. J. H. M.; Weinstein, J. A. On the mechanism of vibrational control of light-induced charge transfer in donor-bridge-acceptor assemblies. *Nat. Chem.* **2015**, 7, 689–695.

(75) Straub, S.; Stubbe, J.; Lindner, J.; Sarkar, B.; Vöhlinger, P. Photoinduced Dynamics of a Diazidocobalt(III) Complex Studied by Femtosecond UV-Pump/IR-to-Vis-Probe Spectroscopy. *Inorg. Chem.* **2020**, 59, 14629–14642.

(76) Clark, R. J. H.; Dines, T. J. Resonance Raman Spectroscopy, and Its Application to Inorganic Chemistry. *New Analytical Methods. Angew. Chem., Int. Ed. Engl.* **1986**, 25, 131–158.

(77) Quinby, M. S.; Feltham, R. D. Infrared spectra of ruthenium derivatives of nitrogen, nitric oxide, and carbon monoxide. Experimental evidence regarding $d\pi\text{-}p\pi$ bonding. *Inorg. Chem.* **1972**, 11, 2468–2476.

(78) Pell, S.; Mann, R. H.; Taube, H.; Armor, J. N. Nitrogen-15-labeled complexes of dinitridopentaammineruthenium(II) chloride. *Inorg. Chem.* **1974**, 13, 479–480.

(79) Lehnert, N.; Tuzek, F. The Reduction Pathway of End-on Coordinated Dinitrogen. I. Vibrational Spectra of $\text{Mo/W-N}_2\text{-NNH}$, and NNH_2 Complexes and Quantum Chemistry Assisted Normal Coordinate Analysis. *Inorg. Chem.* **1999**, 38, 1659–1670.

(80) Bee, M. W.; Kettle, S. F. A.; Powell, D. B. Vibrational spectra of ruthenium and osmium ammine compounds with bridging dinitrogen. *Spectrochim. Acta* **1975**, 31A, 89–100.

(81) Campbell, J. R.; Clark, R. J. H.; Dilworth, J. R. Resonance Raman spectra of the trinuclear dinitrogen-bridged complex $[\{\text{Cl}(\text{PMe}_2\text{Ph})_4\text{Re}(\text{N}_2)\}_2\text{MoCl}_4]$. *J. Chem. Soc., Chem. Commun.* **1980**, 772–773.

(82) Ishida, Y.; Kawaguchi, H. Nitrogen Atom Transfer from a Dinitrogen-Derived Vanadium Nitride Complex to Carbon Monoxide and Isocyanide. *J. Am. Chem. Soc.* **2014**, 136, 16990–16993.

(83) Veige, A. S.; Slaughter, L. G. M.; Lobkovsky, E. B.; Wolczanski, P. T.; Matsunaga, N.; Decker, S. A.; Cundari, T. R. Symmetry and Geometry Considerations of Atom Transfer: Deoxygenation of

- (silox)₃WNO and R₃PO (R = Me, Ph, tBu) by (silox)₃M (M = V, NbL (L = PMe₃, 4-Picoline), Ta; silox = tBu₃SiO). *Inorg. Chem.* **2003**, *42*, 6204–6224.
- (84) Eikey, R. A.; Abu-Omar, M. M. Nitrido and imido transition metal complexes of Groups 6–8. *Coord. Chem. Rev.* **2003**, *243*, 83–124.
- (85) Berry, J. F. Terminal nitrido and imido complexes of the late transition metals. *Comments Inorg. Chem.* **2009**, *30*, 28–66.
- (86) Smith, J. M. Reactive Transition Metal Nitride Complexes. *Prog. Inorg. Chem.* **2014**, *58*, 417–470.
- (87) Meyer, K.; Bendix, J.; Metzler-Nolte, N.; Weyhermüller, T.; Wieghardt, K. Nitridomanganese(V) and-(VI) Complexes Containing Macrocyclic Amine Ligands. *J. Am. Chem. Soc.* **1998**, *120*, 7260–7270.
- (88) Bendix, J. [Cr(N)Cl₄]²⁻: A Simple Nitrido Complex Synthesized by Nitrogen-Atom Transfer. *J. Am. Chem. Soc.* **2003**, *125*, 13348–13349.
- (89) Holland, P. L. Metal-dioxygen and metal-dinitrogen complexes: where are the electrons? *Dalton Trans.* **2010**, *39*, 5415–5425.
- (90) Bond, A. M.; Colton, R.; Humphrey, D. G.; Mahon, P. J.; Snook, G. A.; Tedesco, V.; Walter, J. N. Systematic Studies of 17-Electron Rhenium(II) Carbonyl Phosphine Complexes. *Organometallics* **1998**, *17*, 2977–2985.
- (91) Tran, B. L.; Pinter, B.; Nichols, A. J.; Konopka, F. T.; Thompson, R.; Chen, C.-H.; Krzystek, J.; Ozarowski, A.; Telsner, J.; Baik, M.-H.; Meyer, K.; Mindiola, D. J. A Planar Three-Coordinate Vanadium(II) Complex and the Study of Terminal Vanadium Nitrides from N₂: A Kinetic or Thermodynamic Impediment to N–N Bond Cleavage? *J. Am. Chem. Soc.* **2012**, *134*, 13035–13045.
- (92) Marcus, R. A.; Sutin, N. Electron transfers in chemistry and biology. *Biochim. Biophys. Acta, Rev. Bioenerg.* **1985**, *811*, 265–322.
- (93) Chen, P.; Meyer, T. J. Medium Effects on Charge Transfer in Metal Complexes. *Chem. Rev.* **1998**, *98*, 1439–1478.
- (94) Vlcek Jr., A. The life and times of excited states of organometallic and coordination compounds. *Coord. Chem. Rev.* **2000**, *200–202*, 933–978.
- (95) Bezdek, M. J.; Guo, S.; Chirik, P. J. Terpyridine Molybdenum Dinitrogen Chemistry: Synthesis of Dinitrogen Complexes That Vary by Five Oxidation States. *Inorg. Chem.* **2016**, *55*, 3117–3127.
- (96) McNaughton, R. L.; Roemelt, M.; Chin, J. M.; Schrock, R. R.; Neese, F.; Hoffman, B. M. Experimental and Theoretical EPR Study of Jahn-Teller-Active [HIPTN₃N]MoL Complexes (L = N₂, CO, NH₃). *J. Am. Chem. Soc.* **2010**, *132*, 8645–8656.
- (97) Torres-Alacan, J.; Lindner, J.; Vöhringer, P. Probing the Primary Photochemical Processes of Octahedral Iron(V) Formation with Femtosecond Mid-infrared Spectroscopy. *ChemPhysChem* **2015**, *16*, 2289–2293.
- (98) Shin, J. H.; Bridgewater, B. M.; Churchill, D. G.; Baik, M.-H.; Friesner, R. A.; Parkin, G. An Experimental and Computational Analysis of the Formation of the Terminal Nitrido Complex (η^3 -Cp*)₂Mo(N)(N₃) by Elimination of N₂ from Cp*₂Mo(N₃)₂: The Barrier to Elimination Is Strongly Influenced by the *exo* versus *endo* Configuration of the Azide Ligand. *J. Am. Chem. Soc.* **2001**, *123*, 10111–10112.
- (99) Mehta, P.; Barboun, P.; Herrera, F. A.; Kim, J.; Rumbach, P.; Go, D. B.; Hicks, J. C.; Schneider, W. F. Overcoming ammonia synthesis scaling relations with plasma-enabled catalysis. *Nat. Catal.* **2018**, *1*, 269–275.
- (100) Rouwenhorst, K. H. R.; Kim, H.-H.; Lefferts, L. Vibrationally Excited Activation of N₂ in Plasma-Enhanced Catalytic Ammonia Synthesis: A Kinetic Analysis. *ACS Sustainable Chem. Eng.* **2019**, *7*, 17515–17522.
- (101) Fickes, M. G.; Odom, A. L.; Cummins, C. C. A nucleophilic niobium(V) nitride prepared by isocyanate decarbonylation. *Chem. Commun.* **1997**, *41*, 1993–1994.
- (102) Silvia, J. S.; Cummins, C. C. Two-Electron Reduction of a Vanadium(V) Nitride by CO To Release Cyanate and Open a Coordination Site. *J. Am. Chem. Soc.* **2009**, *131*, 446–447.
- (103) Cozzolino, A. F.; Silvia, J. S.; Lopez, N.; Cummins, C. C. Experimental and computational studies on the formation of cyanate from early metal terminal nitrido ligands and carbon monoxide. *Dalton Trans.* **2014**, *43*, 4639–4652.
- (104) Tran, B. L.; Pink, M.; Gao, X.; Park, H.; Mindiola, D. J. Low-Coordinate and Neutral Nitrido Complexes of Vanadium. *J. Am. Chem. Soc.* **2010**, *132*, 1458–1459.
- (105) Scepianiak, J. J.; Bontchev, R. P.; Johnson, D. L.; Smith, J. M. Snapshots of complete nitrogen atom transfer from an iron(IV) nitrido complex. *Angew. Chem., Int. Ed.* **2011**, *50*, 6630–6633.
- (106) Askevold, B.; Torres Nieto, J.; Tussupbayev, S.; Diefenbach, M.; Herdtweck, E.; Holthausen, M. C.; Schneider, S. Ammonia formation by metal-ligand cooperative hydrogenolysis of a nitrido ligand. *Nat. Chem.* **2011**, *3*, 532–537.
- (107) Cleaves, P. A.; King, D. M.; Kefalidis, C. E.; Maron, L.; Tuna, F.; McInnes, E. J. L.; McMaster, J.; Lewis, W.; Blake, A. J.; Liddle, S. T. Two-Electron Reductive Carbonylation of Terminal Uranium(V) and Uranium(VI) Nitrides to Cyanate by Carbon Monoxide. *Angew. Chem., Int. Ed.* **2014**, *53*, 10412.
- (108) Lambic, N. S.; Sommer, R. D.; Ison, E. A. High-valent nitridorhenium(V) complexes containing PNP ligands: implications of ligand flexibility. *Dalton Trans.* **2018**, *47*, 758–768.
- (109) Buss, J. A.; Cheng, C.; Agapie, T. A Low-Valent Molybdenum Nitride Complex: Reduction Promotes Carbonylation Chemistry. *Angew. Chem., Int. Ed.* **2018**, *57*, 9670–9674.
- (110) Hall, K. A.; Mayer, J. M. Reactions of ML₄Cl₂ (M = Mo, W; L = PMe₃, PMePh₂) with epoxides, episulfides, carbon dioxide, heterocumulenes, and other substrates: a comparative study of oxidative addition by oxygen atom, sulfur atom, or nitrene group transfer. *J. Am. Chem. Soc.* **1992**, *114*, 10402–10411.
- (111) Yonke, B. L.; Reeds, J. P.; Zavalij, P. Y.; Sita, L. R. Catalytic Degenerate and Nondegenerate Oxygen Atom Transfers Employing N₂O and CO₂ and a M^{II}/M^{IV} Cycle Mediated by Group 6 M^{IV} Terminal Oxo Complexes. *Angew. Chem., Int. Ed.* **2011**, *50*, 12342–12346.
- (112) Lohrey, T. D.; Cortes, E. A.; Fostvedt, J. I.; Oanta, A. K.; Jain, A.; Bergman, R. G.; Arnold, J. Diverse Reactivity of a Rhenium(V) Oxo Imido Complex: [2 + 2] Cycloadditions, Chalcogen Metathesis, Oxygen Atom Transfer, and Protic and Hydridic 1,2-Additions. *Inorg. Chem.* **2020**, *59*, 11096–11107.
- (113) Evans, D. F. The determination of the paramagnetic susceptibility of substances in solution by nuclear magnetic resonance. *J. Chem. Soc.* **1959**, 2003–2005.
- (114) Sur, S. K. Measurement of magnetic susceptibility and magnetic moment of paramagnetic molecules in solution by high-field fourier transform NMR spectroscopy. *J. Magn. Reson.* **1989**, *82*, 169–173.
- (115) Haberditzl, W. Advances in Molecular Diamagnetism. *Angew. Chem., Int. Ed. Engl.* **1966**, *5*, 288–298.
- (116) Bain, G. A.; Berry, J. F. Diamagnetic Corrections and Pascal's Constants. *J. Chem. Educ.* **2008**, *85*, 532.
- (117) Bill, E. *Julx 1.4.1 Program for Simulation of Molecular Magnetic Data*; Max-Planck Institute for Chemical Energy Conversion: Mülheim/Ruhr, 2008.